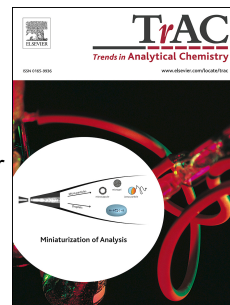# Accepted Manuscript

Transmission Electron Microscopy Analysis of Some Transition Metal Compounds for Energy Storage and Conversion

Chaolun Liang, Fuxin Wang, Wenjie Fan, Wuzong Zhou, Yexiang Tong, Prof.

Please cite this article as: C. Liang, F. Wang, W. Fan, W. Zhou, Y. Tong, Transmission Electron Microscopy Analysis of Some Transition Metal Compounds for Energy Storage and Conversion, *Trends in Analytical Chemistry* (2017), doi: 10.1016/j.trac.2017.02.010.

Transmission Electron Microscopy Analysis of Some Transition Metal Compounds for Energy Storage and Conversion

Chaolun Liang[§], Fuxin Wang[§], Wenjie Fan[§], Wuzong Zhou[#] and Yexiang Tong[§]*

[§] Instrumental Analysis & Research Center, MOE of the Key Laboratory of Bioinorganic and Synthetic Chemistry, The Key Lab of Low-carbon Chemistry & Energy Conservation of Guangdong Province, KLGHEI of Environment and Energy Chemistry, School of Chemistry, Sun Yat-Sen University, Guangzhou, People's Republic of China, 510275

[#] EaStCHEM, School of Chemistry, University of St Andrews, St Andrews, Fife KY16 9ST, United Kingdom

* Corresponding author
E-mail addresses: chedhx@mail.sysu.edu.cn (Prof. Yexiang Tong).

Abstract

Recently, transition metal compounds (TMCs) have been employed as high-performance electrode materials for lithium ion batteries (LIBs) and supercapacitors (SCs) owing to their high specific capacities, high electrical conductivity, and high chemical and thermal stability. While the characterization of electrochemical properties of TMC anodes is well developed, new challenges arise in understanding the structure-property relationships. Transmission electron microscopy (TEM) is a powerful tool for studying microstructural characteristics. With TEM and related techniques, fundamental understanding of how the microstructures affect the properties of the TMC nanostructured anodes can be improved. In this article, the application of TEM in characterization of some typical TMC anode materials optimized through structural engineering, elemental doping, surface modification, defect-control engineering, morphological control, etc. is reviewed. Emphasis is given on analyzing the microstructures, including surface structures, various defects, local

chemical compositions and valence states of transition metals, aimed at illustrating a structure-property relationship. The contribution and future development of the TEM techniques to elucidation of the electrochemical properties of the TMC anodes are highlighted.

1. Introduction

The rapid growth of global population and economy urgently requires alternative and sustainable sources of energy. As the electrical energy can be converted from various forms of energies such as solar energy, wind, tidal and geothermal energy, *etc*, the ability to store electrical energy in a high-efficiency way is the treasure sought by scientists and engineers in the hope of meeting the desires of green power source and sustainable development in the realm of new energies [1, 2]. Lithium-ion batteries (LIBs) and supercapacitors (SCs) are two major electrical energy storage devices [3] that will meet the future demand. LIBs have a leading role in energy storage device for a variety of applications such as portable electronic equipment, electric vehicles, aircrafts and smart electrical grids as well as new energy storage infrastructures, because of their high operational voltage, high-energy density and long cycle life as compared to lead-acid, Ni-Cd and Ni-MH batteries. In spite of the great success in the past two decades, the development of LIBs has reached to a bottleneck recently [4]. SCs, also known as electrochemical capacitors, can provide a bridging function connecting conventional capacitors and rechargeable batteries. SCs can be classified as electric double layer capacitors (EDLC) and pseudocapacitors [5]. EDLCs store charges through absorption/desorption of ions to form electric double layers, while pseudocapacitors involving Faradaic redox reactions exhibit a much higher energy density [6-8].

To fulfill the future requirements, energy storage devices with high power, high energy density, and long cycling stability are highly valued. Electrode materials are the fundamental key components for energy storage devices that largely determine the

electrochemical performance of energy storage devices [9]. In general, electrode materials can be classified into three categories including carbon-based materials, metal compounds and conducting polymers. Recently, on the other hand, transition metal compounds (TMCs) have attracted great interest as they can offer a multitude of electrochemical device opportunities in LIBs and SCs, because of higher theoretical capacity, safety, sustainability, environmental benignity in operation and relatively high electronic conductivity as well as potentially low cost [10, 11]. Most of the developed TMCs such as metal oxides/hydroxides, metal nitrides, and metal sulfides are often used as anode materials in LIBs and SCs.

The properties of anode materials are largely related to their chemical composition, crystallographic structure, surface characteristics, structural defects, electronic structures as well as to a delicate interplay among these factors [12]. With respect to improving the electrochemical performance of TMC anodes, nanostructuring, surface engineering, introducing defects and constructing hybrid structures are the major effective strategies. These structural modifications often provide a large surface area, unique surface and interface structures, more electroactive sites, good electron transport kinetics, hierarchical porous channels and short ionic diffusion distances, resulting in both fast kinetics and high charge/discharge capacities [13]. In this regard, elucidating the detailed microstructure of TMC anodes can help us to explore the structural-property relationships, clarify the mechanisms of the enhancement of the electrochemical properties, and thus facilitate structural optimization of the energy materials oriented for different applications.

TEM is a powerful tool for directly imaging the microstructural characteristics of nanostructured materials. In general, conventional TEM techniques, including bright-field (BF) and dark-field (DF) imaging, select area electron diffraction (SAED), high resolution TEM (HRTEM) and energy dispersive X-ray spectroscopy (EDS), provide information of particle size and morphology, crystal structure, as well as local chemical composition. Over the past ten years, TEM has evolved into a full analytical tool with a sub-angstrom resolution, which allows direct visualization of atomic columns. For example, atomic arrangements in the structural defect sites can be well

resolved using aberration corrected scanning TEM (STEM) or HRTEM. In addition, when coupled with electron energy loss spectroscopy (EELS) and/or EDS, TEM provides the opportunities to obtain electronic structure and elemental distribution information at atomic scale [14]. Nowadays, the state-of-the-art TEM achieves a resolution of about 50 pm and is still extending its functions, which brings new imaging possibilities.

To date, many transition metal oxides and nitrides have been employed as high-performance electrode materials for LIBs and SCs because of their capability of storing lithium through a conversion mechanism. With the help of advanced TEM techniques, the origin of the properties of these anode materials encoded in their microstructures can be elucidated. Several review articles covering such subjects have been published [9, 15-19]. To illustrate a property-structure relationship, the importance of obtaining high resolution images and spectra is obvious. Nevertheless, it is equally important to correctly extract and interpret the information coded in the image and spectrum data. Hence, the purpose of this review will be on analyzing the structural features of a few selected TMC anode materials and understanding their structure-related electrochemical performances. First we will introduce the recent progress of TEM characterization methodologies and their capabilities on investigating electrode materials. Then, the application of different TEM approaches toward the TMC anode materials optimized by various strategies will be described. The main focus will be paid on the structural characteristics including morphologies, surface characteristics, interface structures, crystal defects, chemical composition and electronic structures, which may affect their properties. We hope that our review can provide a fundamental understanding of the structural characteristics of TMC anodes and their electrochemical response, and thus offering a guideline for possible future optimization of their properties.

2. Methodology

2.1 HRTEM

TEM imaging utilizes the information contained in the electron waves exiting from the sample to form an image. In general, by interacting with a specimen, both the amplitude and phase of the incident electrons can be modulated. The modulated electrons carrying with their amplitudes and phases are translated into image contrast by the image formation system [20]. Amplitude contrast results from the amplitude modulation caused by variations in mass-thickness or interference within a crystal [21]. Phase contrast stems from the interaction of the incident electrons with a phase object that introduced a small phase shift to the electron exit-wave. The interference of the electron waves different in phase contributes to the formation of phase contrast image [22]. HRTEM imaging is mainly based on phase contrast, which is sensitive to the atom distribution in the specimen and allows crystal structural imaging at an atomic resolution. To obtain 2D HRTEM images, one often needs to tilt the sample to an on-axis orientation so that the incident beam coincide with a crystallographic axis, enabling the diffraction of various crystal planes and interference between transmitted beam and diffracted beams. Meanwhile, a corresponding diffraction pattern encoding diffracted amplitudes can be obtained [23-25]. The phase preserved in HRTEM images can be combined with the amplitude contained in electron diffraction patterns to discover the atomic structural features [26], although, in comparison with X-ray and neutron diffraction methods, the atomic positions in crystals determined by HRTEM are not so accurate. On the other hand, due to a strong interaction between a high energy electron beam and a solid specimen, atomic scattering amplitudes for electrons are about 10^4 to 10^5 times as large as they are for X-ray and neutrons. Only very small amount of sample are needed to yield meaningful HRTEM images and selected area electron diffraction (SAED) patterns. Consequently, nanocrystallites and local structures at sub-nanometer scale in particles, e.g. individual defects, can be

imaged.

With regard to the investigation of energy material, HRTEM can provide valuable information about the internal structure of the electrode materials such as crystallographic orientations, defects, surface and interface structures, which are closely related to the crystal growth mechanisms and the possible process of electrochemical reactions. For example, Shao-Horn *et al.* [27] reported the visualization of atomic columns in $LiCoO_2$ electrode using focal series HRTEM images, which can be applied in determining the ordering of lithium and vacancies in transition metal oxides. Liu *et al.* [28] revealed the dynamic lithiation process at the surface of single crystal silicon with atomic resolution. Recently, it has been shown that the cation and oxygen deficiency in transitional metal oxides, such as manganese oxides, titanium oxides, vanadium oxides, iron oxides and tin oxides, can be confirmed by using HRTEM [29-34]. However, it should be noted that one may run the risk of error in correlating HRTEM image to the atomic structures of specimens, since the contrast in HRTEM images changes dramatically with specimen thickness and defocus, owing to the so-called multiple scattering effect, and is also strongly dependent on the resolution of the microscopy [35, 36].

2.2 HRSTEM

Using a finely focused electron probe to scan across a defined region of specimen, signals in STEM imaging are generated by the elastic scattering between the incident electron beam and the sample. The electron scattering angles vary according to the sample characteristics such as structure, atomic number and composition. By adapting the suitable camera length and convergence angle, the rim of the scattered electrons can reach to specific annular detectors [37]. In this way, elements with different atomic numbers contained in the sample can be distinguished by detecting the intensity of scattered electrons hitting the annular detector. Therefore, STEM imaging can provide directly interpretable incoherent contrast reflecting atomic numbers,

which is contrary to HRTEM imaging that the contrast is sensitive to both of the defocus value of imaging forming lens and of the sample thickness. The annular detectors can be cataloged according to their collection angles. Annular dark field (ADF) detector, positioned around the central bright field detector, is used to gather electrons scattered at angles in the range of 10-50 mrad, aiming at detecting heavy elements. HAADF-STEM imaging is based on large angle Rutherford scattering (larger than 50–60 mrad) [38, 39] of fast electrons. The intensity of the projected image is approximately proportional to the square of the atomic number of the element contained in the sample, known as Z-contrast imaging [40]. Areas with high intensity in a HAADF-STEM projection of a nanocrystal represent a region with a higher average atomic number [41]. As a result, the HAADF technique is most sensitive to heavy elements, and relative chemical information can also be obtained from HAADF-STEM images. However, both ADF and HAADF STEM imaging exclude the electrons scattered by light elements [39]. Recently, the newly developed annular bright field (ABF) detector that positioned within the illumination cone of focused electron beam permits direct visualization of light elements such as oxygen and nitrogen atomic columns as well as heavy atoms at the same time [42, 43]. Coupling with different annular detectors, STEM imaging plays a crucial role in the study of crystal and crystal defects, as well as the imaging of individual atoms. For example, atomic columns of heavy elemental dopants and light elemental atoms, such as In-doped ZnO [44], N-doped graphene [45], Eu, Si co-doped AlN [46], *etc.,* can be well resolved using STEM mode. Applications of HRSTEM on energy materials over the past decade have mainly involved visualization of atom sites in cathode materials, *e.g*. $LiCoO_2$ [47], $LiMn_2O_4$ [48] and $LiFePO_4$ [49, 50]. Furthermore, recent reports on anode materials including $Li_4Ti_5O_{12}$ [51], FeF_2 [52] and SnO [53] have demonstrated that STEM imaging can reveal electrochemical lithium storage mechanisms in atomic scale.

2.3 EDS and EELS

Apart from basic imaging techniques, other element-specific techniques, such as EDS, electron energy loss spectrum (EELS) and energy filtered TEM (EFTEM) are also powerful tools for clarifying the chemical structure, chemical bonding and valence state as well as chemical environment of the TMC anode materials. Both EDS and EELS are based on the inelastic scattering of fast electrons with atoms in a material [54]. During the scattering process, a fast electron transfers energy ΔE to excite an electron to an unoccupied state. The lost energy ΔE of the fast electron can be determined through an EELS spectrometer and then be used to generate EFTEM images. After exciting the inner shell electrons, the outer shell electrons are de-excited by emitting characteristic (X-ray) photons, which can be detected by an EDS detector. Consequently, using EELS spectrometer and EDS detector, the energy loss electrons and X-rays yielded by the interaction between electron beam and the probed species enable qualitative and quantitative element analysis [55].

EDS is often combined with STEM that acquires signals one at a time, which allows line profiles or elemental mapping from a specific line or a region of interest in the specimen. This technique is particularly suitable for heavy elements with high fluorescence yield [56]. With the development of aberration corrected STEM that improves the spatial resolution and sensitivity in STEM techniques to sub-Ångstrom scale , it has been demonstrated that chemical imaging at atomic scale can be obtained [57-61].

EFTEM permits analysis of a wider range of elemental distribution, in particular for light elements because the elemental maps obtained by selecting core-loss ionization edges at specific energies provide higher geometrical signal collection efficiency, better chemical sensitivity and energy resolution as compared to EDS [62]. Spatial resolution of better than 1 nm and detection limit of less than a monolayer of elements are readily attainable in EFTEM [63, 64]. In order to give quantitative images of the distribution of a specific element in EFTEM, the background generated by plural-scattering should be calculated and then subtracted to leave the edge

intensity. Such background removal procedure is more complicated in comparison with the intense peaks and low background level in EDS.

EELS can be utilized to obtain information on the composition, valence state, chemical bonding information and electronic structures of solid state materials [65]. When combined with STEM, site-specific measurements of local compositions and electronic structure can be obtained by EELS. Spatial resolution down to single atom scale is attainable by spectrum imaging [66]. EELS plays a unique role in studying the charge storage process as both chemical and bonding information of the electrode materials can be obtained. Recent STEM-EELS investigations on graphene [67], single crystal Si [28], BP [68], Fe_2O_3 [69, 70], and α-MoO_3 [71] have demonstrated its capability in revealing the electrochemical lithiation process and the conversion reaction mechanisms. It should be noted that since EELS is an analytical technique based on inelastic scattering of fast electrons, multiple scattering of the inelastic signal restricts the electronic structural analysis to a specimen thickness less than 70 nm for most materials [72].

3. Application of HRTEM and HRSTEM

3.1 Oxygen deficient Fe_2O_3 nanorods

Hematite (α-Fe_2O_3) holds great promise as a negative electrode for asymmetric supercapacitors (ASCs) because of its large theoretical specific capacitance and suitable working window in negative potential [73, 74]. However, pure hematite materials are of limited application potential due to the low conductivity and power density [33, 75]. Oxygen vacancies in α-Fe_2O_3 can serve as shallow donors, and introducing oxygen vacancies into α-Fe_2O_3 can improve its donor density and surface properties, thus enhancing the electrochemical performance of the materials [33]. Hence, investigation on the oxygen-deficient structure provides a fundamental

understanding on the relationship between defect chemistry and the electrochemical properties of α-Fe_2O_3.

Several TEM studies have shown that oxygen deficiency generated an ordering superlattice structure in α-Fe_2O_3. For example, Cvelbar *et al.* [76] reported the formation of a modulated structure of α-Fe_2O_3 induced by oxygen vacancies. HRTEM and corresponding FFT showed a superlattice structural feature with ordering of the oxygen-vacancy planes. Using HRSTEM imaging, Lee *et al.* [77] found a periodic contract caused by vacancy-ordering planes in oxygen deficiencies α-Fe_2O_3 nanowires. Similarly, experimental and simulated HRTEM investigation revealed a long-range oxygen-vacancy ordering planes in α-Fe_2O_3 nanowires and nanobelts [78, 79]. The occurrence of these superstructures could be explained by the formation of oxygen-vacancy-ordered planes. Such oxygen vacancies results in the p-type conductivity of α-Fe_2O_3 [78].

In other studies, stacking faults and twin defects were found in the synthesized Fe_2O_3 nanostructures, in which no oxygen-vacancy-ordering was observed. This might be ascribed to the increase of oxygen vacancies density and their migration that destroy the modulated structure [77, 80]. Recently, Lu *et al.* [33] reported the planar defect microstructure of oxygen-deficient α-Fe_2O_3 nanorods and their electrochemical properties as anode for SCs. The morphology of α-Fe_2O_3 nanorods obtained through thermal decomposition of β-FeOOH under a N_2 atmosphere (denoted as N-Fe_2O_3) was studied by BF TEM. (as shown Fig. 1). The porous nanorod is composed of a bundle of nanowires about 8 nm in diameter, indicating that the nanorod is polycrystalline. The corresponding SAED pattern (the inset of Fig. 1a) that looks like a diffraction pattern of single crystal suggests the crystals in the rod are well orientated. In other words, the "single crystal"-like diffraction pattern could be explained by the overlapping SAED patterns originated from individual single crystalline nanowires with approximately the same orientation. The Fourier filtered reconstructed HRTEM image (as shown in Fig. 1c) clearly shows the zigzag arrangements of the lattice fringes, indicating the presence of planar defects (stacking faults) perpendicular to the (113) planes. In addition, the intensity profile (Fig. 1e) of the defect region in Fig. 1d

revealed the uneven d-spacing of the (100) planes. The observed lattice distortions and the variation of the (100) d-spacing could possibly be related to the oxygen vacancy defect sites caused by the oxygen deficient environment during the synthesis process [77]. Furthermore, the presence of Fe^{2+} species were detected by X-ray photoelectron spectroscopy (XPS), which suggests that oxygen vacancies were formed in N-Fe_2O_3 [33]. Therefore, it can be speculated that the observed planar defects could be attributed to the oxygen vacancies induced by thermal treatment under a N_2 atmosphere. These oxygen deficient α-Fe_2O_3 nanorods exhibited enhanced capacitance and cycling stability, which is possibly due to the formation of oxygen vacancies that serve as shallow donors [33]. Electrochemical impedance experiments were further conducted by Lu *et al.* [33], which confirmed the enhancement of the donor density in the N-Fe_2O_3 as compared with pure Fe_2O_3.
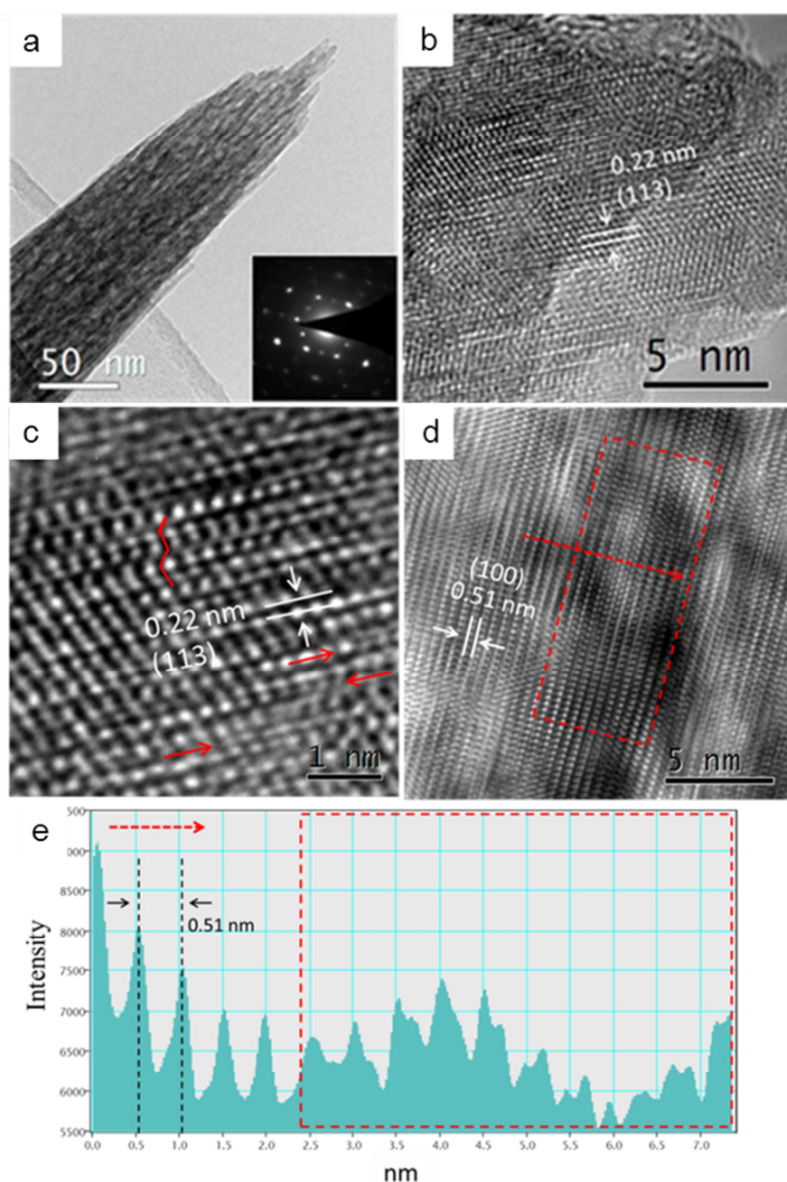
Figure 1. TEM investigation of N-Fe$_2$O$_3$ nanorods. (a) Bright field image and the corresponding SAED pattern (the inset). (b) HRTEM image. (c) Enlarged HRTEM image showing defects. The zig-zag arrangement of the lattice fringes indicated by the red lines can be ascribed to the planar defects (stacking faults). The red arrow shows the dislocation defects. (d) HRTEM image of the defect structure, showing the contrast variation induced by the defects. (e) Intensity profile of the red square region, indicating the uneven d-spacing of the N-Fe$_2$O$_3$ defect structure. (Reproduced with permission of [33])

3.2 Polyhedral Fe$_3$O$_4$ nanoparticles

Fe$_3$O$_4$ has been considered as a promising anode material for LIBs because of its high theoretical capacities (924 mA h g^{-1}), low-cost and environmental benignity [81, 82]. Its structure is cubic with the unit cell parameter, a = 0.839 nm, space group

13

Fd3m. Nanosized Fe_3O_4 crystals with well-defined shapes have attracted great attention because of the size and surface effects [3, 83], as well as the shape effect. Table 1 shows the first discharge capacity of Fe_3O_4 anode materials with different morphologies. As the shape, that determines the surface termination and surface atomic arrangement, is crucial to the electrochemical properties [84, 85], it is necessary to acquire information on the crystal morphology of Fe_3O_4 nanoparticles (NPs).

Table 1 The specific capacity of Fe_3O_4 anode differ in morphology

Morphology	Current density	First discharge capacity	Reference
Fe_3O_4 nanoparticle clusters	$0.1 \, A \, g^{-1}$	$850 \, mA \, h \, g^{-1}$	[86]
Fe_3O_4 hollow nanoparticle aggregates	$0.1 \, A \, g^{-1}$	$800 \, mA \, h \, g^{-1}$	[87]
Fe_3O_4 nanocrystals	0.2 C	$1200 \, mA \, h \, g^{-1}$	[88]
Fe_3O_4 rhombic dodecahedra	0.2 C	$1147 \, mA \, h \, g^{-1}$	[89]
Fe_3O_4 submicrospheres	$0.1 \, A \, g^{-1}$	$910 \, mA \, h \, g^{-1}$	[90]
Grapecluster-like Fe_3O_4@C/carbon nanotube nanostructures	$0.1 \, A \, g^{-1}$	$926 \, mA \, h \, g^{-1}$	[91]
Commercial Fe_3O_4 nanoparticles	$0.1 \, A \, g^{-1}$	$790 \, mA \, h \, g^{-1}$	[92]
hierarchical Fe_3O_4 microspheres/graphene	$0.2 \, A \, g^{-1}$	$1336 \, mA \, h \, g^{-1}$	[93]
Fe_3O_4 polyhedral nanoparticles	$0.1 \, A \, g^{-1}$	$1067 \, mA \, h \, g^{-1}$	[94]

To date, a variety of TEM techniques have been utilized to obtain the 3D morphological features of nanocrystal with size less than 100 nm. The routine characterization techniques include BF-TEM and electron diffraction. The shape and the type of exposed facets of nanocrystals can be identified by a combined analysis of the interplane angles between the facets, TEM images and electron diffraction

14

patterns of the crystals. For example, α-Fe_2O_3 nanocrystals with hexagonal bipyramid shape and rhombohedral shape were identified by measuring the angles between each two surface planes in BF image and indexing the corresponding SAED pattern [95]. Another approach for examining 3D morphologies is DF-TEM imaging. Čaplovičová *et al.* [96] developed a weak beam dark field technique to characterize the 3D shape of TiO_2 nanocrystals. The thickness changes depicted in the weak beam dark field images revealed that the anatase crystals consist of tetragonal bypyramidal morphology. Furthermore, the shape and the exposed surface planes can be estimated on the base of projected two-dimensional HRTEM images. Stroppa *et al.* [97] evaluated the three dimensional morphology of Sb doped SnO_2 nanocrystals by combined use of experimental HRTEM image, multislice simulated HRTEM images, and Wulff construction as well as surface energy ab initio calculations. The approaches mentioned above are based on the principle of crystallographic analysis of a series of 2D projections and with the assumption that the surface structure is not reconstructed. An alternative technique to identify the 3D morphology is electron tomography, which enables the reconstruction of 3D shape from 2D projections through a mathematical algorithm. Xu *et al.* [98] reported the 3D morphology reconstruction of octahedral CeO_2 nanocrystals using TEM tomography BF tilt series from $-50°$ to $+70°$ at a $5°$ angular increment. However, the missing wedge artifacts have been considered as one of the most important challenges in the field of electron tomography [54].

Recent reports have shown the characterization of the 3D morphology and electrochemical properties of Fe_3O_4 NPs by utilizing electron crystallography. For example, Zheng *et al.* [99] determined the truncated octahedral shape of Fe_3O_4 NPs around 12 nm based on the [100], [101] and [111] projected HRTEM images. Xu *et al.* [89] performed a geometrical analysis for Fe_3O_4 nanocrystals using HRTEM and electron diffraction, revealing that the rhombic dodecahedral shaped crystals were enclosed by highly active {110} planes. These crystals have shown superior electrochemical properties, which can be ascribed to the higher surface energy.

15

Similarly, Cao *et al.* [88] reported Fe_3O_4 nano-cubes that delivered an initial discharge capacity of 1200 mA h g $^{-1}$ at 0.2 C.

Recently, we demonstrated the morphological characterization of Fe_3O_4 NPs around 12 nm [94]. The surface terminations and the shape were estimated by electron crystallography. It should be noted that it is difficult to perform orientation adjustment due to the finite size and sample drift. However, careful control of the TEM conditions and a wide observation up to 900 individual NPs with different view directions allow us to examine the particle shape and surface terminations. Projected images of the Fe_3O_4 particles along the [100], [110] and [111] zone axes of the cubic unit cell are displayed in Fig. 2(a1), (b1) and (c1) respectively. Fourier filtering was employed to extract the lattice fringe information. Surface terminations were determined while different crystal facets were parallel to the viewing direction. It should be noted that a single HRTEM image is a 2D projection of a 3D particle. It is still questionable whether the observed smooth surface is a profile image of a facet or an image of an edge of the crystal [100]. Examination of multiple HRTEM images along different zone axes by rotating the crystal can overcome this problem.
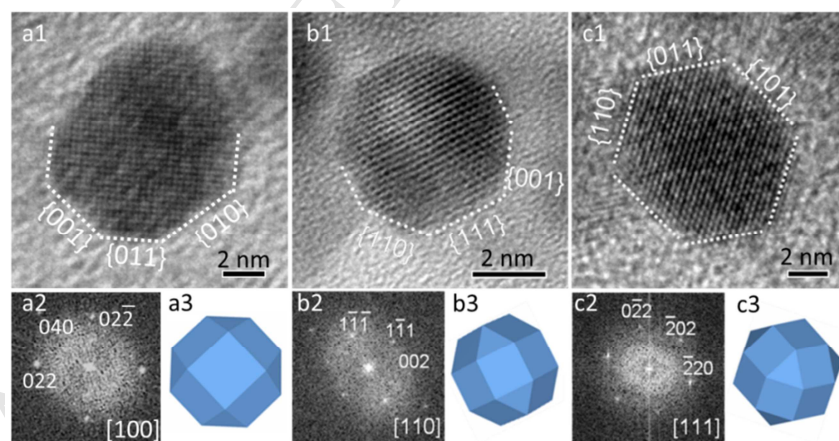
Figure 2. HRTEM images and geometrical models of polyhedral Fe_3O_4 nanoparticles viewed along (a1) [100], (b1) [110] and (c1) [111] zone axes. Panel (a2, b2, c2) are the corresponding Fast Fourier Transform (FFT) patterns. Panel (a3, b3, c3) are the corresponding projected shapes of the 3D structural model. (Reproduced with permission of [94])

Based on the crystallographic data obtained from different projections, an idealized geometrical structure of 26-facet rhombicuboctahedron that consists of 6

{100}, 12 {110} and 8 {111} facets was proposed (as shown in Fig. 2a3-c3). There are 24 identical vertices and 52 edges on each rhombicuboctahedron, offering low-coordinated atoms that can have a strong impact on the chemical activity. Particles with truncated octahedron morphology were also identified by imaging the surface facets in profile, as shown in Fig. 3.
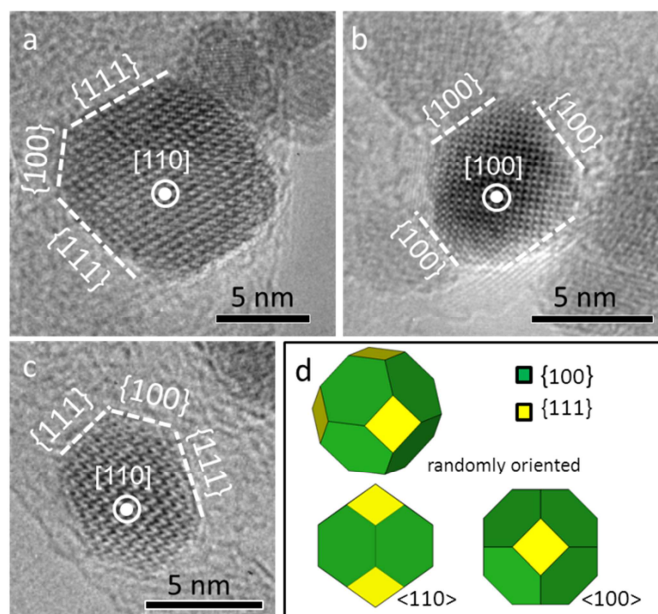
Figure 3. HRTEM images of truncated octahedral Fe_3O_4 nanoparticles projected along (a) [110], (b) [100], and (c) [110] orientations. (d) Geometric models of the truncated octahedron enclosed with {100} and {111} facets. (Reproduced with permission of [94])

According to the morphological features and the growth rates of different crystallographic orientations, a possible growth mechanism of the NPs was proposed. Fig. 4 illustrated the shape transformation of the polyhedral Fe_3O_4 NPs. Firstly, the Fe_3O_4 nuclei tend to form an octahedron bound by the most stable {111} planes. Later, glycol (PEG) that acts as a capping agent absorbs on the high energy {100} planes, resulting in a 14-facet truncated octahedral shape. With increasing reaction time, the particle would grow further into a 26-facet polyhedron as a result of the slow growth of both {100} and {110} planes. Therefore, the final shape of the Fe_3O_4 NPs is a mixture of series of 14-facet truncated octahedra and 26-facet polyhedra. Galvanostatic charge-discharge measurements showed that the NPs delivered a high initial discharge capacity of 1067 mA h g^{-1} [94], which could be attribute to their

small size and abundant exposure of edges and corners in the multi-faceted polyhedral structures, offering low-coordinated atoms that act as active sites for lithium storage.
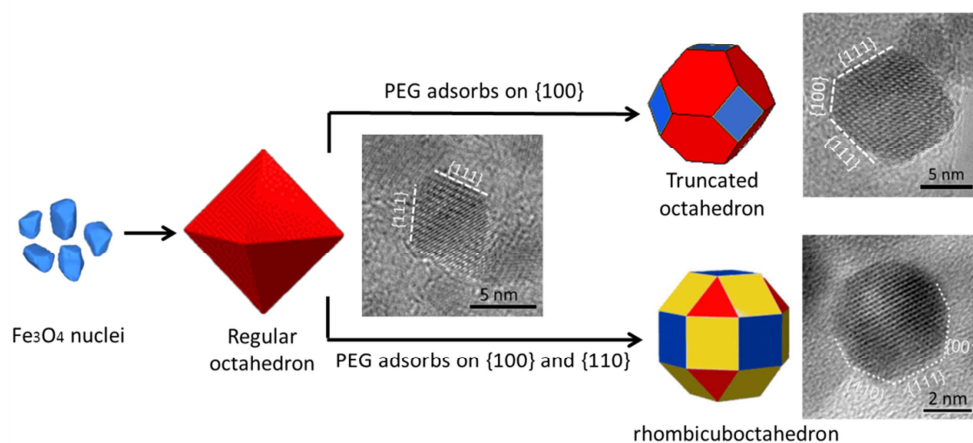

Figure 4. Schematic illustration of the proposed growth mechanism that lead to the formation of truncated octahedral and rhombicuboctahedral Fe_3O_4 nanoparticles. {110}, {111} and {100} facets are coloured yellow, red and blue, respectively. (Reproduced with permission of [94])

3.3 Defects in TiO$_2$

TiO_2 is an inexpensive and electrochemically stable semiconductor. However, as an electrode material for SCs, TiO_2 suffers from relatively low electrical conductivity and poor electrochemical activity [101]. Recent reports demonstrated that introducing defects in TiO_2 can address these limits and thus improve specific capacitance and stability of TiO_2 materials [102, 103]. The detailed microstructural investigation is critical to understand how the defect structure influences the electrical conductivity and electrochemical activity of TiO_2. The defects characterization is a typical problem solved by TEM. Fröschl *et al.* [104] carried out HRTEM studies on defective TiO_2 nanorods before and after cycling. The aberration-corrected high-resolution TEM image revealed hillocks, terraces and surface corrugations as well as lattice bending, which offer openings to Li diffusion channels and thus facilitating the reversible Li incorporation. Chen *et al.* [105] presented HRTEM analysis of the surface

hydrogenated TiO$_2$ nanocrystals. A thin layer of hydrogenated disordered surface on the crystalline TiO$_2$ electrode was discovered by HRTEM. Similarly, Qiu *et al.* [106] investigated the microstructure of hydrogenated rutile TiO$_2$ nanoparticles. Fourier filtered HRTEM images indicated the hydrogenation induced crystal defects such as dislocation lines and grain boundaries, which can play an important role in Li-ion diffusion efficiency. It was found that these hydrogenated TiO$_2$ crystals can facilitate the charge transfer process and capacity retention.

Another example of characterizing hydrogenated TiO$_2$ was presented by Lu [102]. In the study, HRTEM and HAADF-STEM results visually demonstrated the presence of dislocation defects in the hydrogen heat treated TiO$_2$ (denoted as H- TiO$_2$).
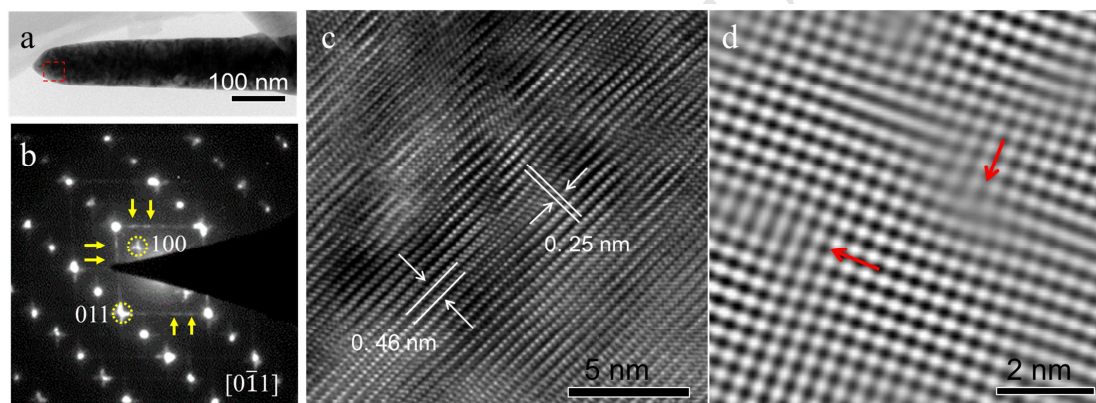
Figure 5. (a) Bright field image, (b) SAED pattern, (c) HRTEM image and (d) HAADF-STEM image after Fourier filtered reconstruction of the H-TiO$_2$ nanowire.

BF TEM image (Fig. 5a) shows the rod-like structure of TiO$_2$. The corresponding SAED pattern as shown in Fig. 5b can be indexed to the rutile phase TiO$_2$ single crystal structure (JCPDS No. 65-0192) with high crystallinity. However, the shape and intensity of diffraction spots indicate that it is an imperfect crystal. The streaks in the SAED pattern (as indicated by yellow arrows) reveal a high density of lattice defects in the structure. HRTEM image (Fig. 5c) collected at the top of nanowires edge (red square region) shows the lattice fringes of (100) and (011) planes of the rutile structure, suggesting that TiO$_2$ grew along the [100] direction and maintained the same phase after hydrogen treatment. Moreover, HRTEM analysis indicated the

characteristics of defects. The uneven d-spacing and distortions of the lattice fringes can be clearly observed. Domains with different image contrast can also be identified. These findings suggest the existence of high density defects in the structure. For qualitative study of the crystal defects, HAADF-STEM imaging and Fourier filtering were performed. Fig. 5d shows an inverse Fourier filtered transform image viewing along the [0$\bar{1}$1] direction. As the bright spots correspond to the atomic columns of Ti, the defect sites can be clearly identified. In addition, the distribution of atomic displacements in the defect core (as shown by red arrows) can be discerned, confirming the presence of dislocation defects. Based on the TEM analysis, it was found that hydrogenation treatment generated a high density of dislocation defects. Combined with XPS studies that identified the formation of Ti^{3+} ions [102], it is speculated that the dislocation defects could possibly be attributed to the oxygen vacancies.

3.4 S-doped Bi_2Te_3

Tuning the electronic structure of Bi_2Te_3 through introducing dopants represents an effective approach to further enhance their physical-chemical properties [107]. Recently, it was demonstrated that S-doped Bi_2Se_3 crystals exhibited enhanced electrochemical performance as anode for lithium-ion batteries. It is believed that the sulfur dopants can improve the electrical conductivity [108]. The effect of doping is well known, but the crystal structure after doping and the distributions of the dopants are objects of many intensive studies.

Z-contrast imaging technique is a powerful tool for the characterization of doped microstructures. Signals in Z-contrast image is proportional to about the square of the average atomic number of the probed sample volume. Shibata *et al.* [109] demonstrated the atomic-scale observation of yttrium-doped grain boundary in alumina using aberration-corrected Z-contrast STEM. As shown in Fig. 5, the doped

Y atomic columns are clearly imaged with very strong contrast and form a monoatomic layer structure in the core of the boundary. Z-contrast imaging was utilized to investigate the microstructure of $Bi_2Te_3(Se_3)$ compounds such as Bi_2Te_3 [110], Bi_2Se_3 [111], Mn-doped Bi_2Te_3 [112] and $Bi_2Te_{2.7}Se_{0.3}$ [113]. Although quintuple layer consisting five alternating Bi and Te(Se) atomic layers can be well resolved, the distribution of dopant atoms needs to be further clarified.
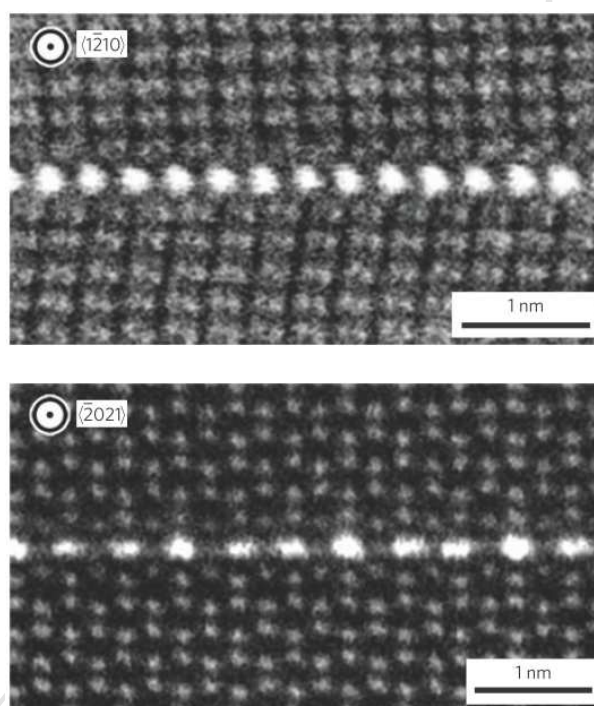
Figure 6. Z-contrast STEM images of the Y-doped grain boundary observed from two orthogonal directions parallel to the interface plane. (Reproduced with permission of [98])

In our recent study, HAADF-STEM imaging was employed to investigate the distribution of S dopants in Bi_2Te_3 [107]. Contrast intensity analysis was used to estimate the preferential occupation sites of dopants. For the analysis of location and distribution of S dopants in Bi_2Te_3, the [100] zone axis of Bi_2Te_3 is selected and aligned accurately as in this orientation Bi and Te atomic columns can be viewed separately. Fig. 7a shows a Z-contrast STEM image viewed along the [100] direction. Brighter contrast corresponds to the atomic columns of Bi, while relatively weaker

contrast represents the atomic columns of Te. Intensity line profiles of S-doped Bi_2Te_3 and simulated image based on undoped-Bi_2Te_3 were compared. For pure Bi_2Te_3, peak intensities of every Te atomic columns are uniform as is shown in the simulation profile (Fig. 7d). By contrast, three Te columns exhibit different intensities in the experimental intensity profile (Fig. 7c). As the weaker intensity of Te1 columns can be mainly attributed to their lower average Z compared with bare Te columns, such relatively weak contrast indicates that S dopants partially replace Te atoms in the Te1 columns. This is in common with the results obtained by Dycus *et al.* [113] in which it is determined that Se dopants in Bi_2Te_3 preferentially occupy Te1 sites.
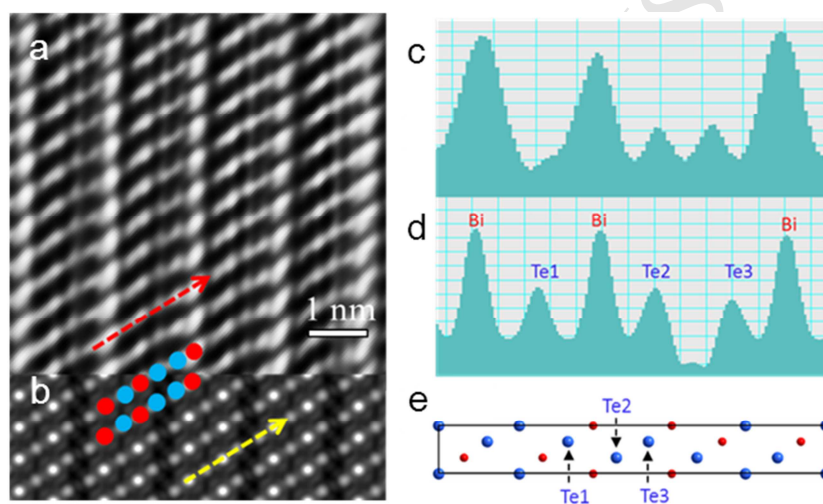
Figure 7. (a) FFT filtered HAADF-STEM image of S-doped Bi_2Te_3. (b) Simulated HAADF-STEM image of undoped-Bi_2Te_3. (c) Intensity profile of FFT filtered STEM image of S-doped Bi_2Te_3 along the red arrow. (d) Intensity profile of the undoped-Bi_2Te_3 image along the yellow arrow. (e) Unit cell structure model of Bi_2Te_3. Te1 refers to the Te atomic columns between Bi columns, while Te2 and Te3 columns are neighbored on the van der Waals gap (Reproduced with permission of [107])

To further evaluate the distribution of S dopants, estimations of the intensity profiles in a number of regions of interest (ROI) were performed. The result (as shown in Fig. 8b) shows that the contrast of all Te1 columns is weaker than that of Te2 and Te3 columns, suggesting that S atoms preferentially substitute Te in the Te1 sites. Besides, the uneven intensities in Te2 and Te3 columns suggest that S dopants

should be randomly distributed in such Te sites. Intensity profile analysis reveals that S prefers to occupy the Te1 sites until it is completely substituted, which is in agreement with previously reported results [113, 114]. In summary, the intensity variation of the Te column in HAADF-STEM images can be explained by the partial and uneven substitution of S. Te columns with least contrast intensity correspond to the preferential occupation sites of S atoms. Although S atoms do not have sufficient contrast to be seen in the image owning to the low Z, the sulfur-containing columns are visible as weaker contrast compared with pure Te columns.
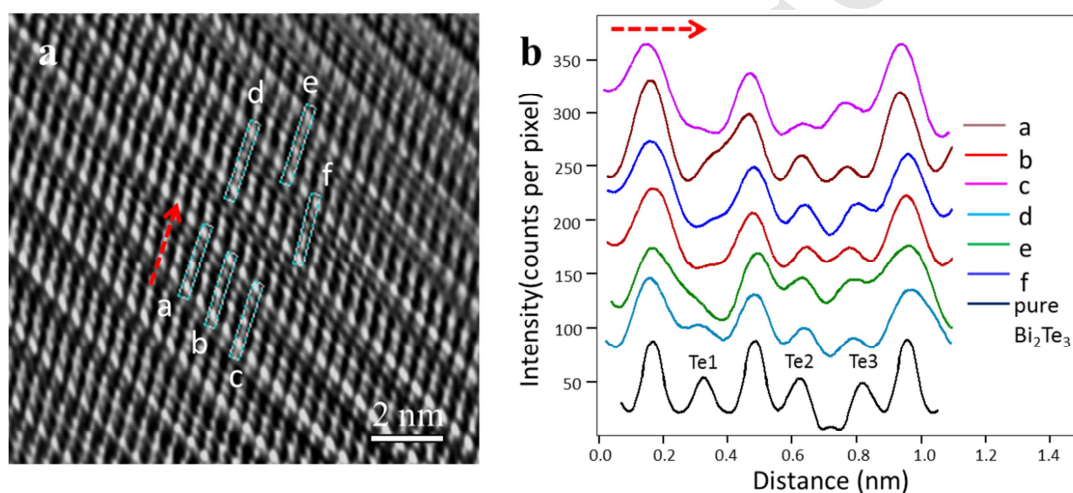
Figure 8. (a) STEM image of S-doped Bi_2Te_3. Regions of interest (ROI) for contrast intensity analysis are marked as "a-f". (b) Intensity profiles of the ROI in (a). Red arrows show the analysis direction of intensity profiles. (Reproduced with permission of [107])

4. Application of EELS and elemental mapping

4.1 Microstructural evolution of TiO_2 and TiN

During the charge-discharge cycles, electrochemical charge storage reactions occur at surface or in a thin-layer region of active materials (several tens of

nanometers from the surface) [3]. Therefore, the understanding of the charge-discharge mechanisms and the electrochemical reaction between TMC electrodes and electrolyte largely relies on their surface structural characteristics, especially the surface composition, active sites, oxidation states and elemental distributions [115]. Elemental mapping and EELS analysis are now widely used for the analysis of these surface and interface related issues.

TiO$_2$ is a promising alternative anode to carbonaceous materials in LIBs, as it can provide superior safety, chemical stability and non-toxicity. Gao *et al.* [116] reported a new electrochemical reaction mechanism by observing the lithiation process of TiO$_2$ nanotube. HRTEM revealed the nano-islands Li$_2$Ti$_2$O$_4$ crystal with cubic structure was formed at the surface layer of TiO$_2$ nanotube during the lithiation. EELS analysis showed that the lithiation started with the oxidation state of Ti^{4+} reduced to Ti^{3+}, resulting in the formation of amorphous Li$_x$TiO$_2$ intercalation compound. The further intercalation of Li ions in TiO$_2$ nanotubes stimulated an amorphous to crystalline phase transformation. This phase transformation was found to be associated with the local inhomogeneity in Li distribution, which was revealed by STEM-EELS elemental mapping. Based on in situ chemical and structural analyses, the authors proposed a new reaction mechanism for the lithiation behavior of amorphous TiO$_2$ nanotubes.

TiN holds great promise as an electrode material for SCs due to its superior electrical conductivity (4000 ~ 55500 S/cm) and mechanical stability [117, 118]. However, previous studies found that TiN electrode performed in alkaline electrolyte solution suffered from substantial capacitance loss (28% retention of initial capacitance after 400 cycles), while the underlying degradation mechanism remains unclear [119, 120]. Chemical identification for the TiN electrode after cycling test can help to understand the origin of the instability of TiN nanowires. Here, we demonstrated the spectrum imaging investigation to reveal the mechanism causing the capacitance loss of TiN. In addition, the difference between EELS and EDS spectrum imaging results are compared and discussed.

Fig. 9a shows a HAADF-STEM image of TiN nanowires after 3000 cycles.

Nanowires with rough surface can be observed. STEM-EDS mapping was performed and the spectrum image pixels were summed to produce the spectra (as shown in Fig. 9b) that shows the characteristic N Kα (392 eV), O Kα (523 eV) and Ti Kα (4508 eV) peaks. Additionally, STEM-EDS elemental mapping (as shonw in Fig. 9c-e) illustrates that not only Ti and N, but also O are uniformly distributed in the nanowires. The presence of O implies that the instability of TiN electrode may be due to the formation of oxides during cycling. Nevertheless, it should be noted that in EDS mapping the elemental distribution is generated by integrating the peak intensity with a given width of integration window. For the best element detectability, the integration width for the peak of interest should be 1.2 times the full-width-at-half-maximum (FWHM) [121]. In this case, the integration energy windows for N Kα peak and Ti Lα peak (456 eV) can contribute to the integrated intensity of the nearby O Kα peak, which may produce artifacts that the O element map displayed as homogeneously distributed. Although we set a mapping window from a region near the N Kα peak containing no element X-ray peak and subtract the map to remove background contribution, the resultant elemental map still cannot provide further spatial distribution details.
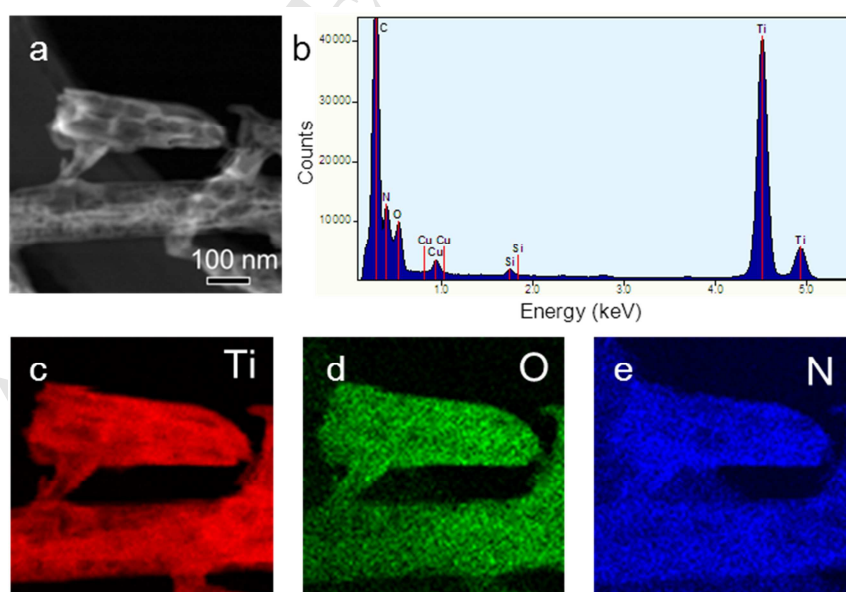
Figure 9. (a) HAADF-STEM image of a representative TiN nanowire. (b) Summed spectrum corresponding to (a). (c-e) STEM-EDS elemental maps of Ti, O and N, respectively.

In order to accurately identify the chemical composition and elemental

distribution, STEM-EELS analysis were carried out. STEM-EELS can collect and storage an entire spectrum at every pixel to generate a data set, which can later produce elemental maps at a given energy and construct spectra from a selected image region. Through spectrum-image data processing, the distributions of Ti, N and O in a TiN nanowire are obtained (as shown in Fig. 10a). It can be seen that the surface of the nanowires are enriched with O. In addition, it is clearly in the color-mixed map that pink regions contain both Ti and N, whereas both Ti and O are collocated in surface, indicating the formation of oxide shells. Fig. 10b shows a summed spectrum from a surface region of the TiN nanowire, in which the characteristic N-K edge, Ti-L$_{2,3}$ edges and O-K edge can be identified.
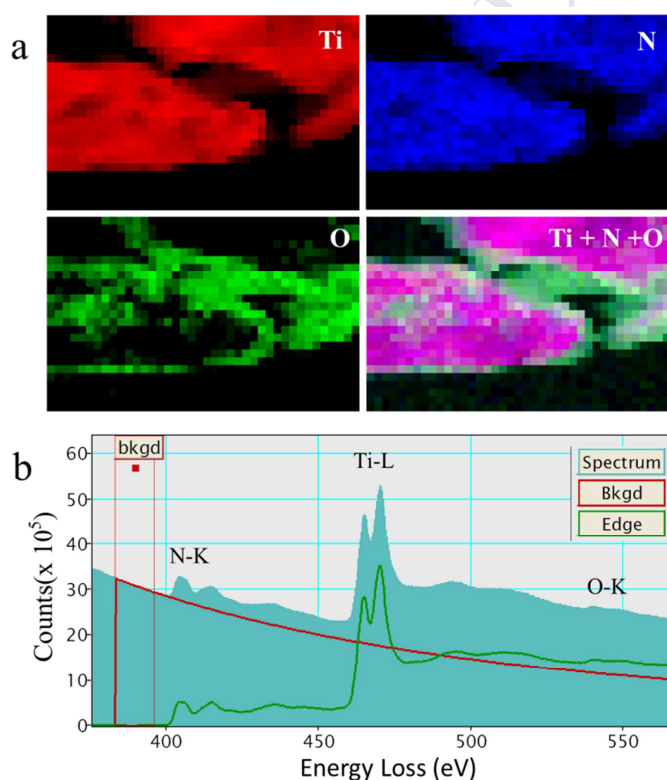
Figure 10. (a) STEM-EELS elemental map of TiN nanorod, showing the distribution of Ti, N, and O. (b) Summed spectrum extracted from the spectrum image pixels.

Furthermore, to compare the valence state of Ti in surface and core region, spectrum data from the surface and inner part of the nanowire (as shown in Fig. 11a) were extracted and further processed by power-law background subtraction and

second derivation. In the second derivative spectrum (as shown in Fig. 11e and Fig. 11f), the onset of N-K edge can be fixed to 401 eV. Thus, the chemical shifts of Ti-L$_{2,3}$ white lines can be identified.
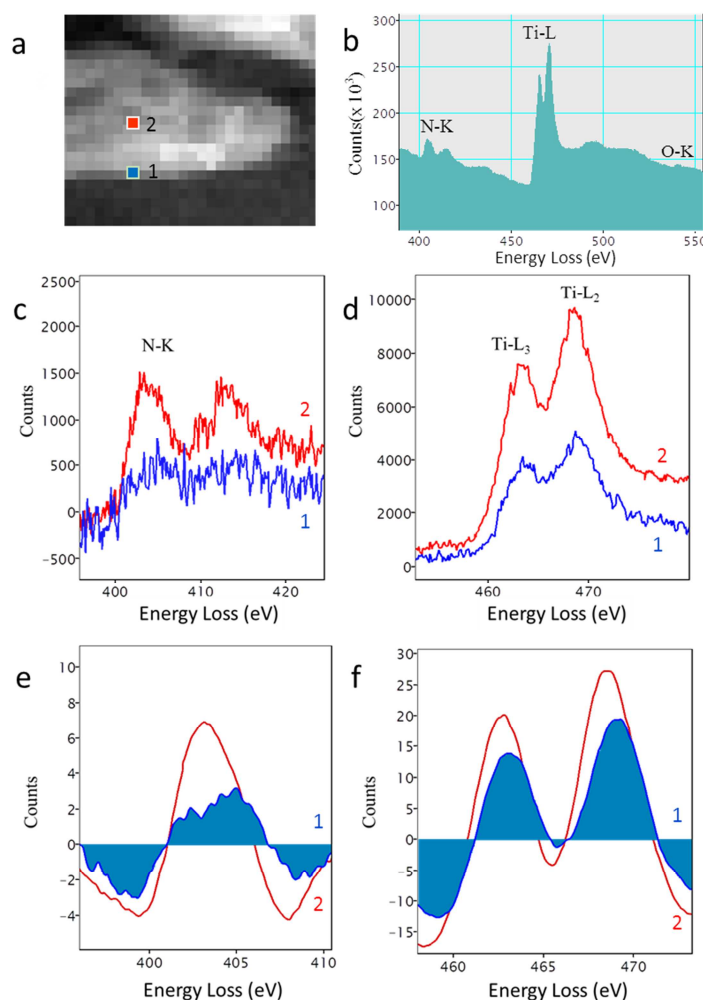
Figure 11. (a) HAADF image, (b) Summed spectrum extracted from the surface region of TiN nanorod, (c, d) EELS spectra extracted from the surface (blue lines) and inner region (red lines), showing the N-K edge and the Ti-L$_{2,3}$ edges, respectively. (e, f) Second derivative spectra corresponding to (c) and (d), respectively.

Comparing with the inner region, there is a chemical shift of 0.4 eV to higher energies in the spectra extracted from the surface of H-TiO$_2$, suggesting a higher oxidation state. This result indicates the formation of Ti^{4+} in the surface as a result of oxidation after cycling. Therefore, EELS analysis revealed that the instability of TiN

electrode should be due to the formation of the electrochemically less active TiO_2 layer on TiN surface [117, 118]. In summary, the mechanism causing the capacitance loss for the TiN nanowires electrode was revealed. STEM-EELS has been demonstrated to be a technique which can be very reliable in forms of both mapping and spectroscopy data. On the contrary, STEM-EDS is easier to generate elemental distribution maps which can be made without prior knowledge of specimen composition. However, some experimental conditions such as sample thickness, peak overlap, background processing, detector counting rates and dead times can induce erratic fluctuations which may lead to misinterpreted results [62].

4.2 Carbon coated TiN

Surface coating has been proven to be important and efficient in suppressing the interfacial side reactions, alleviating the decomposition of the electrolyte, improving ionic and electronic conductivities and buffering the volume change upon cycling [122]. Elemental mapping has been conducted for characterizing the chemical distribution of many coated structures, for example, $TiN–BaTiO_3$ core–shell particles [123], MnO_2/TiN nanotube coaxial arrays [124], TiN–porous carbon [125], TiN@Si core–shell nanorods [126], $TiO_2–C/MnO_2$ core-shell nanowires [127] and so on. These anode materials exhibited improved cycling and rate performance, which can be ascribed to the homogeneously distributed surface layers with high conductivity and stability. However, while using STEM-EDS mapping, care should be taken to specimens containing N and Ti, because the N Kα peak (392 eV) and Ti Lα peak (456 eV) were so close that the resultant map could be questionable. On the other hand, the spatial distribution of Ti and N can be well differentiated by EELS through detecting the ionization edges of Ti L-edge (485 eV) and N-K edge (401 eV).

Fig. 12 shows an example of identifying the elemental distribution of carbon coated TiN nanowire using EFTEM imaging. A three-window method was employed by selecting the core-loss ionization edges of C-K edge at 284 eV, N-K edge at 401

eV and Ti-L$_{2,3}$ edge at 485 eV [128]. The width of the energy windows ΔE of carbon, nitrogen and titanium was set to be 10 eV. Fig. 12(c-e) shows the C-K, Ti-L$_{2,3}$ and N-K core-loss images. It can be seen that the nanorods are of TiN core-C shell type. The thickness of the outer carbon layer is about 1 ~ 2 nm, which is in consistent with the HRTEM result. EFTEM analysis evidenced a continuous carbon enriched layers on the surface of TiN nanowires, which could stabilize the electrochemically active TiN nanoawire arrays electrode without sacrificing their performances [129].
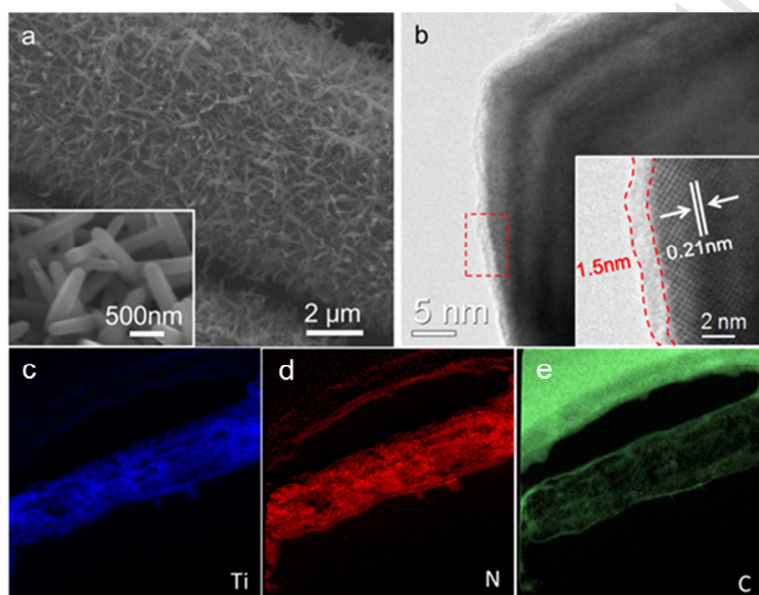
Figure 12. (a) SEM image, showing the size and morphology of TiN nanowires that were grown on carbon fibers. (b) HRTEM image of TiN@C, showing the carbon layer with thickness of 1.5 nm, (c-e) EFTEM image obtained by a three windows method, showing the elemental distribution of Ti, N and C, respectively. (Reproduced with permission of [129])

4.3 MnO$_{2-x}$ nanorods

MnO$_2$ is an attractive pseudocapacitive material with high theoretical specific capacitance [130]. However, its poor electrical conductivity (10^{-5} -10^{-6} S cm^{-1}) severely restricts its practical application as high-performance electrode material for SCs. Hydrogenation treatment is a major approach to enhance the intrinsic conductivity of transition metal oxides [102, 131]. To better understand the effect of hydrogenation treatment, it is important to study how the valence state of Mn is

modified in the hydrogen treated structure.

In the EELS core-loss spectrum, the integral intensity ratio of the L_3 ($2p^{3/2} \rightarrow 3d$) and L_2 ($2P^{1/2} \rightarrow 3d$) excitation peaks is sensitive to the change in the valence states of transition metal cations [132-135]. Therefore, the oxidation states of transition metal cations can be identified by measuring the integrated intensities of $L_{2,3}$ edges. In addition, the electron-energy-loss near-edge structures (ELNES) of the O-K edge are related to the electronic states in the unoccupied conduction band in the case of transition metal oxides, which can also be used to obtain the information about the valence state of transition metal cations.

One such example is the EELS analysis for the hydrogenation induced mixed valence MnO_{2-x} nanorod as demonstrated by Zhai *et al.*[136]. EELS experiment was conducted at an energy range containing the $Mn-L_{2,3}$ and the O-K edges, with an energy resolution of 0.9 eV. The background was subtracted by a power-law fitting in the pre-edge region of the spectrum. The oxidation state of Mn ions were evaluated according to the intensity ratio of $Mn-L_{2,3}$ edges and the EELS fine structure of O-K edges. The TEM and EELS instrument was firstly calibrated in both TEM-diffraction mode and STEM mode using standard MnO_2 and Mn_3O_4 samples so as to compare with the literature reported values [132, 133, 137, 138]. Fig. 13 shows a typical EELS spectra of the untreated MnO_2 nanorods and hydrogenated MnO_2 (denoted as H-MnO_2) nanorods acquired in TEM-diffraction mode. The dominant sharp peaks observed in the EELS spectra are the L_3 and L_2 ionization edges of Mn. The L_3/L_2 integral intensity ratio of the untreated MnO_2 nanorods was calculated to be 2.2, which can be related to the oxidation state of Mn^{4+} [139]. The L_3/L_2 integral intensity ratio of the H-MnO_2 was calculated to be 3.2, suggesting that not only Mn^{4+} but also Mn^{2+} and Mn^{3+} should exist in the sample. Besides, the ELNES of O-K edge can be used to analysis the valence state of Mn since the 3d and 4s states of Mn hybridized with O 2p orbitals [140]. As compared with MnO_2, the relative intensity between the prepeak around 530 eV (labelled as *peak a*) and the second peak at 5-10 eV above threshold (labelled as *peak b*) in the H-MnO_2 spectrum is smaller than that in the

MnO_2 spectrum. Since the intensity of the prepeak is related to the occupancy of the Mn 3d orbitals, the reduced intensity of prepeak in H-MnO_2 suggests a reduction of the oxidation state of Mn. This result further indicated that the H-MnO_2 should be a mixed valence compound [141, 142].

Furthermore, the valence state of Mn in the surface and central part of the nanorod were analyzed in STEM mode. STEM-EELS analysis was applied to five hydrogen treated MnO_2 nanorods, and a high reproducibility of the spectra features was found. The EELS spectra from the surface of H-MnO_2 nanorods (Fig. 14b) showed that the L_3/L_2 intensity ratio was 3.1, indicating that there are Mn^{2+}, Mn^{3+} and Mn^{4+} cations in the surface of H-MnO_2 NRs. Meanwhile, the L_3/L_2 intensity ratio of the central part of H-MnO_2 nanorods, which combined the core and surface information of the rods, was calculated to be 2.8. This suggests that more Mn^{4+} existed in the central part of the nanorod. All these clear differences in EELS spectra demonstrated a variation of the valence state of the Mn ions. Based on TEM results, new structure Mn_3O_4 (other than normal MnO_2) can be identified within surface of nanorod, indicating the hydrogenation induced surface reduction of MnO_2. The superior conductivity and capacitive performance of H-MnO_2 were confirmed by cyclic voltammetry, charge-discharge measurements and electrochemical impedance spectroscopy [136]. According to the above results, the coexistence of multivalent Mn and the surface charge storage play an important role in accelerating the kinetics of the surface redox reactions as well as electronic and ionic transport properties, and thus enhancing its electrochemical performances.
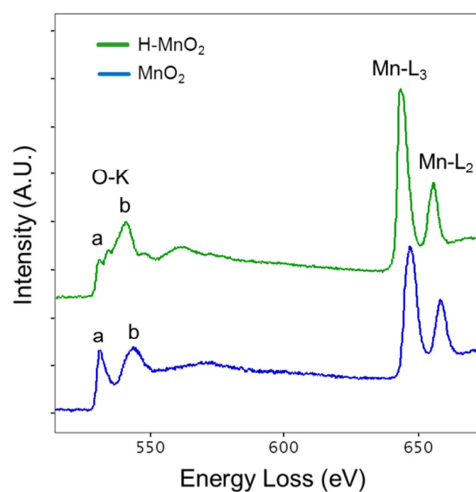
Figure 13. EELS spectra of untreated MnO_2 nanorods and H-MnO_2 nanorods.
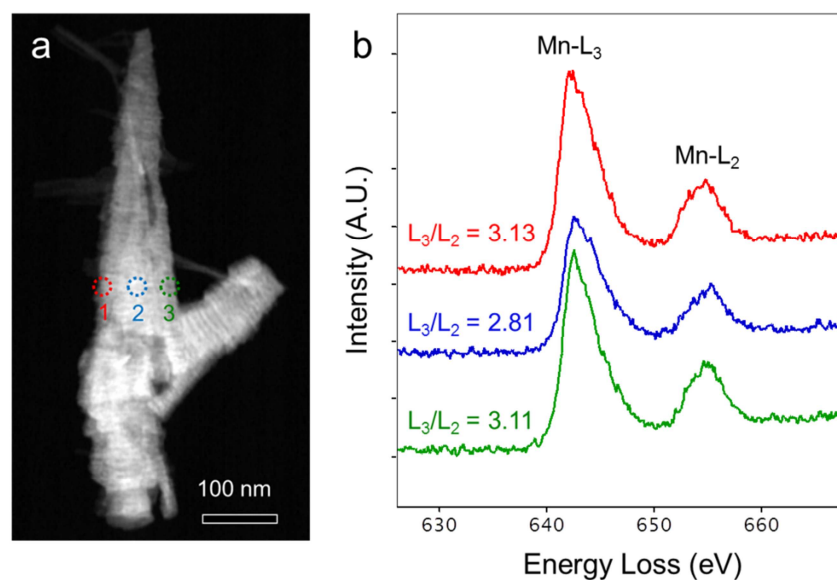
Figure 14. (a) HAADF-STEM image of the H-MnO_2 nanorod. (b) EELS spectra from the surface and central part of the H-MnO_2 nanorod, showing the intensity of Mn-$L_{2,3}$ edges.

4.4 V_6O_{13}

Mixed-valence vanadium oxides are promising electrode materials for pseudocapacitors [143]. The incorporation of dopants to vanadium oxides can introduce multivalent vanadium cations into the structure and thus improve the capacitive performance. Characterizing the doping elements is one of the most

32

significant challenges in TEM.

Several reports showed the TEM investigation on the structural characteristics of the doped vanadium oxides. Using selected area electron diffraction analysis, Lee *et al.* [144] demonstrated the inhomogeneous doping of VO_2 nanowires with W. Zhao *et al.* [145] compared the morphology of V_2O_5/TiO_2 nanoparticle before and after sulfur doping. BF TEM showed that the S-doped V_2O_5/TiO_2 nanoparticles were more uniform in morphology and less agglomerated than the undoped sample. Asayesh-Ardakani *et al.* [146] reported the aberration corrected HRSTEM imaging of W doped $V_{1-x}O_2$ nanorod. The substitution of W with V atoms in the crystal structure was confirmed by atomic resolution HAADF image. EDS elemental mapping further revealed the homogeneous dispersion of W in the nanowire.

Zhai *et al.* [147] demonstrated an example of investigating the microstructures and chemical composition of S-doped V_6O_{13} nanowires via HRTEM, STEM-EDS and EFTEM mapping. Fig. 15a shows a HRTEM image of the S-doped V_6O_{13} nanowire. However, this lattice resolved HRTEM image does not provide evidences for sulfur dopants in V_6O_{13}. Another example also showed that HRTEM do not usually reflect the doping effects. Ishiwata *et al.* [148] conducted HRTEM analysis for Cr and Ti doped V_2O_3 nanocrystals, in which doping induced defects were not observed. Therefore, elemental mapping is desired to obtain the chemical information of the doped vanadium oxides. STEM-EDS was employed to identify the distribution of the S dopants. The sulfur elemental map (Fig. 15b) defined clearly the spatial distribution of S in an individual nanowire, which confirmed that sulfur is uniformly distributed. Due to the fact that the V Lα peak (510 eV) and O Kα-peak (523 eV) are overlapped, the resultant O Kα signals may be false and invalidate the elemental distribution map. Therefore, it is still necessary to employ EFTEM imaging to confirm the elemental distribution of S-doped V_6O_{13}.
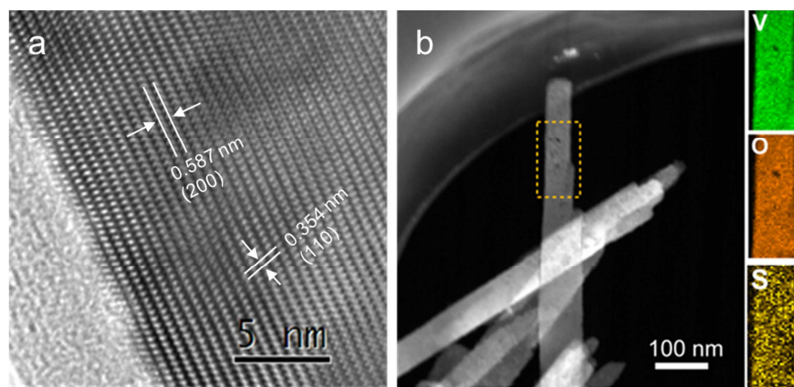
Figure 15. (a) Lattice resolved HRTEM image collected at the edge of a S-doped V_6O_{13} nanowire. (b) HAADF-STEM image of S-doped V_6O_{13} nanowires and the STEM-EDS mapping of V, O and S obtained from the selective area in the dashed box. (Reproduced with permission of [147])

Fig. 16 shows that V, O and S are homogeneously distributed in the nanowires, which are in consistent with the STEM-EDS results. Chemical composition studied by TEM successfully confirmed the introduction of sulfur dopants in the V_6O_{13} nanowires. Combined with electrochemical analysis, it is found that sulfur-doping reduces the charge-transfer resistance and increase the ion diffusion coefficient [147].
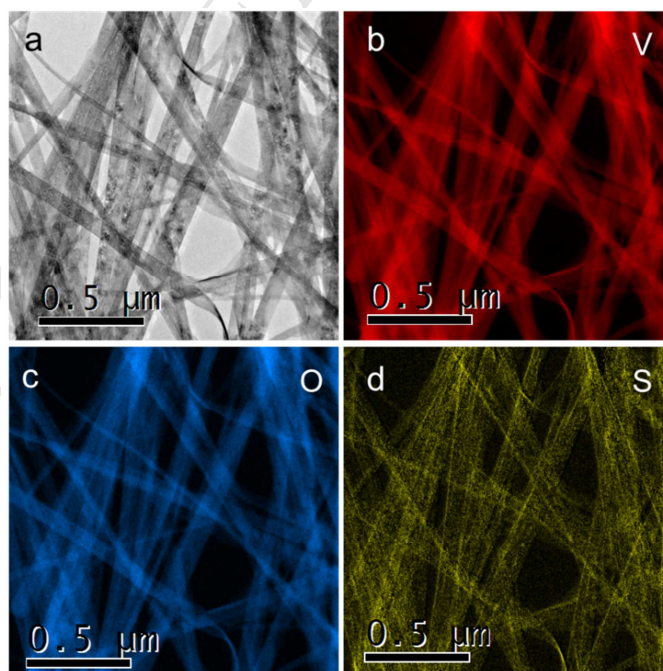
Figure 16. (a) TEM image of S-doped V_6O_{13} nanowires, (b-d) EFTEM image obtained by three-window method using V-$L_{2,3}$,O-K and S-K edges, respectively.

5. Conclusion and outlook

TiO$_2$, TiN, MnO$_2$, V$_6$O$_3$, α-Fe$_2$O$_3$, Fe$_3$O$_4$ and Bi$_2$Te$_3$ have been extensively investigated as anodes for LIBs and SCs. Various strategies, including morphological control, surface modification, defect-control engineering, elemental doping, *etc*., have been developed to improve the performance of these anode materials. As research on boosting the electrochemical properties of anode materials through structural engineering continues, the ability to image and characterize the microstructural features of the structurally modified anode materials has become increasingly important. TEM has been proven to be quite useful and powerful in the investigation on TMC nanostructured anodes. The advanced TEM allows us to determine the structure of a complex surface and interface, to detect dopant atoms in the lattice, to measure the surface valence state and generate chemical composition distribution maps. In this review, we summarize the contributions of the TEM techniques to understand the electrochemical properties of TMC anodes, with emphasis on analyzing and interpreting the structural information coded in image and spectrum data.

The most standard procedures for microstructure investigation, including BF, SAED and HRTEM, provide crystallographic information, lattice structures and even three dimension morphological description of nanoparticles, offering opportunities for the examination of their facet-dependent electrochemical properties. Also, morphological analysis based on SAED and HRTEM can offer insights into the shape evolution and growth mechanisms of nanocrystals.

Besides the routine applications of morphologies and lattice structure characterization, one of the most outstanding contributions of TEM on developing TMC anodes is to observe the structural changes in nano- or even atomic-scale in defect-control engineering. For instance, the identification of defect structures obtained by thermal treatment under H$_2$ or N$_2$ atmosphere has verified the capability

of offering valuable information about the lattice distortions by HRTEM imaging. Moreover, advanced TEM techniques like HAADF-STEM has demonstrated the ability to detect and characterize not only the atomic arrangements in the structural defect sites, but also the distribution of dopants in the atomic columns, all of which being closely associated with charge carrier concentration, conductivities, and transport properties in TMC anodes.

Additionally, it has been shown that the elemental mapping by means of STEM-EDS and EFTEM provides considerably better chemical information when probing a complex structure. However, the use of more than one technique should be applied in order to validate the elemental maps. Also, background signals should be carefully subtracted in order to get complementary results, especially for elements with low concentrations. Apart from imaging techniques such as HRTEM and chemical mapping, EELS spectroscopic analysis plays a crucial role in understanding the behavior of TMC anode because it can provide reliable valence state detection on one hand, and better chemical sensitivity on the other. In particular, EELS shows great advantages in revealing the possible chemical process in the charge-discharge cycles by offering the opportunity to monitor the valence state of transition metal elements.

The successful structural analyses of morphologies, surface characteristics, interface structures, crystal defects, atomic distributions, chemical composition and valence states as well as electronic structures have demonstrated that TEM can make a significant contribution to understand the charge-discharge mechanisms, to elucidate the origin of the superior properties and to explore the structure-properties relationships. Nevertheless, concerning the accurate investigation on the structural features of TMC anodes, special attention should be paid on sample preparation, particular imaging conditions and image contrast analysis to avoid the over-interpretation of the TEM data. All of the examples mentioned above are highly dependent on the competent operational skills and knowledge on data interpretation and analysis. Still, TEM is considered as one of the most powerful tools for the determination of complex structures. While combining the state-of-the-art monochromized and Cs-corrected TEM/STEM with in-situ techniques, the

36

micro-mechanisms for the superior electrochemical properties of TMC anodes are continuing to be further uncovered, and the achievement of high performance novel anodes is expected.

Acknowledgements

Appendix Abbreviations

ABF	annular bright field
ADF	annular dark field
ASCs	asymmetric supercapacitors
BF	bright-field
DF	dark-field
EDS	energy dispersive X-ray spectroscopy
EDLC	electric double layer capacitors
EELS	electron energy loss spectroscopy
EFTEM	energy filtered TEM
ELNES	electron-energy-loss near-edge structures
FWHM	full-width-at-half-maximum
HAADF	high angle annular dark field
HRTEM	high resolution transmission electron microscopy
LIBs	lithium-ion batteries
NPs	nanoparticles

PEG	polyethylene glycol
SAED	select area electron diffraction,
SCs	supercapacitors
SEM	scanning electron microcopy
STEM	scanning transmission electron microscopy
TEM	transmission electron microscopy
TMC	transition metal compound
XPS	X-ray photoelectron spectroscopy

References

[1] J.M. Tarascon, M. Armand, Issues and challenges facing rechargeable lithium batteries, Nature 414 (2001) 359-367.

[2] M. Armand, J.M. Tarascon, Building better batteries, Nature 451 (2008) 652-657.

[3] J. Jiang, Y. Li, J. Liu, X. Huang, C. Yuan, X.W. Lou, Recent advances in metal oxide-based electrode architecture design for electrochemical energy storage, Adv. Mater. 24 (2012) 5166-5180.

[4] Z. Song, H. Zhou, Towards sustainable and versatile energy storage devices: an overview of organic electrode materials, Energy Environ. Sci. 6 (2013) 2280-2301.

[5] P. Simon, Y. Gogotsi, Materials for electrochemical capacitors, Nat. Mater. 7 (2008) 845-854.

[6] C. Liu, F. Li, L.-P. Ma, H.-M. Cheng, Advanced materials for energy storage, Adv. Mater. 22 (2010) E28-E62.

[7] C. Liu, Z. Yu, D. Neff, A. Zhamu, B.Z. Jang, Graphene-based supercapacitor with an ultrahigh energy density, Nano Lett. 10 (2010) 4863-4868.

[8] J.R. Miller, P. Simon, Electrochemical capacitors for energy management, Science 321 (2008) 651-652.

[9] M.S. Balogun, W. Qiu, W. Wang, P. Fang, X. Lu, Y. Tong, Recent advances in

metal nitrides as high-performance electrode materials for energy storage devices, J. Mater. Chem. A 3 (2015) 1364-1387.

[10] P. Poizot, S. Laruelle, S. Grugeon, L. Dupont, J.M. Tarascon, Nano-sized transition-metal oxides as negative-electrode materials for lithium-ion batteries, Nature 407 (2000) 496-499.

[11] J. Cabana, L. Monconduit, D. Larcher, M.R. Palacín, Beyond intercalation-based Li-ion batteries: the state of the art and challenges of electrode materials reacting through conversion reactions, Adv. Mater. 22 (2010) E170-E192.

[12] D. Batuk, M. Batuk, A.M. Abakumov, J. Hadermann, Synergy between transmission electron microscopy and powder diffraction: application to modulated structures, Acta Crystallogr. Sect. B: Struct. Sci. 71 (2015) 127-143.

[13] M. Yu, W. Qiu, F. Wang, T. Zhai, P. Fang, X. Lu, Y. Tong, Three dimensional architectures: design, assembly and application in electrochemical capacitors, J. Mater. Chem. A 3 (2015) 15792-15823.

[14] D.A. Muller, Structure and bonding at the atomic scale by scanning transmission electron microscopy, Nat. Mater. 8 (2009) 263-270.

[15] J.L. Rouvière, E. Prestat, P. Bayle-Guillemaud, M.D. Hertog, C. Bougerol, D. Cooper, J. Zuo, Advanced semiconductor characterization with aberration corrected electron microscopes, J. Phys.: Conf. Ser. 471 (2013) 012001.

[16] S. Carenco, S. Moldovan, L. Roiban, I. Florea, D. Portehault, K. Valle, P. Belleville, C. Boissiere, L. Rozes, N. Mezailles, M. Drillon, C. Sanchez, O. Ersen, The core contribution of transmission electron microscopy to functional nanomaterials engineering, Nanoscale 8 (2016) 1260-1279.

[17] L. Ji, Z. Lin, M. Alcoutlabi, X. Zhang, Recent developments in nanostructured anode materials for rechargeable lithium-ion batteries, Energy Environ. Sci. 4 (2011) 2682-2699.

[18] X.H. Liu, J.Y. Huang, In situ TEM electrochemistry of anode materials in lithium ion batteries, Energy Environ. Sci. 4 (2011) 3844-3860.

[19] H.B. Wu, J.S. Chen, H.H. Hng, X. Wen Lou, Nanostructured metal oxide-based materials as advanced anodes for lithium-ion batteries, Nanoscale 4 (2012)

2526-2542.

[20] J.C.H. Spence. High-resolution Electron Microscopy, Oxford University Press, New York, 2003.

[21] D.B William, C.B. Carter, Transmission Electron Microscopy — a Text Book for Materials Science, Plenum Press, New York, 1996.

[22] B. Fultz, J. Howe, Diffraction Contrast in TEM Images, Transmission Electron Microscopy and Diffractometry of Materials, Springer Berlin Heidelberg, Berlin, Heidelberg, 2013, 349-427.

[23] T. Ohsuna, Z. Liu, O. Terasaki, K. Hiraga, M.A. Camblor, Framework determination of a polytype of zeolite beta by using electron crystallography, J. Phys. Chem. B 106 (2002) 5673-5678.

[24] B. Lu, F.H. Li, Z.H. Wan, H.F. Fan, Z.Q. Mao, Electron crystallographic study of $Bi_4(Sr_{0.75}La_{0.25})_8Cu_5O_y$ structure, Ultramicroscopy 70 (1997) 13-22.

[25] T.E. Weirich, X. Zou, R. Ramlau, A. Simon, G.L. Cascarano, C. Giacovazzo, S. Hovmoller, Structures of nanometre-size crystals determined from selected-area electron diffraction data, Acta Crystallogr. Sect. A 56 (2000) 29-35.

[26] S.J.L. Billinge, I. Levin, The problem with determining atomic structure at the nanoscale, Science 316 (2007) 561-565.

[27] Y. Shao-Horn, L. Croguennec, C. Delmas, E.C. Nelson, M.A. O'Keefe, Atomic resolution of lithium ions in $LiCoO_2$, Nat. Mater. 2 (2003) 464-467.

[28] X.H. Liu, J.W. Wang, S. Huang, F. Fan, X. Huang, Y. Liu, S. Krylyuk, J. Yoo, S.A. Dayeh, A.V. Davydov, S.X. Mao, S.T. Picraux, S. Zhang, J. Li, T. Zhu, J.Y. Huang, In situ atomic-scale imaging of electrochemical lithiation in silicon, Nat. Nano 7 (2012) 749-756.

[29] B.P. Hahn, J.W. Long, D.R. Rolison, Something from nothing: enhancing electrochemical charge storage with cation vacancies, Acc. Chem. Res. 46 (2013) 1181-1191.

[30] J.Y. Shin, J.H. Joo, D. Samuelis, J. Maier, Oxygen-deficient $TiO_{2-\delta}$ nanoparticles via hydrogen reduction for high rate capability lithium batteries, Chem. Mater. 24 (2012) 543-551.

[31] X. Lu, D. Zheng, T. Zhai, Z. Liu, Y. Huang, S. Xie, Y. Tong, Facile synthesis of large-area manganese oxide nanorod arrays as a high-performance electrochemical supercapacitor, Energy Environ. Sci. 4 (2011) 2915-2921.

[32] H. Li, P. He, Y. Wang, E. Hosono, H. Zhou, High-surface vanadium oxides with large capacities for lithium-ion batteries: from hydrated aerogel to nanocrystalline $VO_2(B)$, V_6O_{13} and V_2O_5, J. Mater. Chem. 21 (2011) 10999-11009.

[33] X. Lu, Y. Zeng, M. Yu, T. Zhai, C. Liang, S. Xie, M.S. Balogun, Y. Tong, Oxygen-deficient hematite nanorods as high-performance and novel negative electrodes for flexible asymmetric supercapacitors, Adv. Mater. 26 (2014) 3148-3155.

[34] N. Li, K. Du, G. Liu, Y. Xie, G. Zhou, J. Zhu, F. Li, H.M. Cheng, Effects of oxygen vacancies on the electrochemical performance of tin oxide, J. Mater. Chem. A 1 (2013) 1536-1539.

[35] P.J. Goodhew, J. Humphreys, R. Beanland. Electron microscopy and analysis (third edition). Taylor & Francis press, London, 2001, 106-107.

[36] W. Z. Zhou, Defect fluorite-related superstructures in the Bi_2O_3-V_2O_5 system. J. Solid State Chem. 76 (1988) 290-300.

[37] E.M. James, N.D. Browning, Practical aspects of atomic resolution imaging and analysis in STEM, Ultramicroscopy 78 (1999) 125-139.

[38] S.J. Pennycook, D.E. Jesson, A.J. McGibbon, P.D. Nellist, High angle dark field STEM for advanced materials, J. Electron Microsc. 45 (1996) 36-43.

[39] E. Carlino, TEM for characterization of semiconductor nanomaterials, Transmission Electron Microscopy Characterization of Nanomaterials, Springer Berlin Heidelberg, 2014, 89-138.

[40] S.J. Pennycook, Structure determination through Z-contrast microscopy, Advances in Imaging and Electron Physics, Elsevier 2002, 173-206.

[41] B. Goris, A. De Backer, S. Van Aert, S. Gómez-Graña, L.M. Liz-Marzán, G. Van Tendeloo, S. Bals, Three-dimensional elemental mapping at the atomic scale in bimetallic nanocrystals, Nano Lett. 13 (2013) 4236-4241.

[42] S.D. Findlay, N. Shibata, H. Sawada, E. Okunishi, Y. Kondo, Y. Ikuhara, Dynamics of annular bright field imaging in scanning transmission electron

microscopy, Ultramicroscopy 110 (2010) 903-923.

[43] M. de la Mata, C. Magen, J. Gazquez, M.I.B. Utama, M. Heiss, S. Lopatin, F. Furtmayr, C.J. Fernández-Rojas, B. Peng, J.R. Morante, R. Rurali, M. Eickhoff, A. Fontcuberta i Morral, Q. Xiong, J. Arbiol, Polarity assignment in ZnTe, GaAs, ZnO, and GaN-AlN nanowires from direct dumbbell analysis, Nano Lett. 12 (2012) 2579-2586.

[44] H. Schmid, E. Okunishi, T. Oikawa, W. Mader, Structural and elemental analysis of iron and indium doped zinc oxide by spectroscopic imaging in Cs-corrected STEM, Micron 43 (2012) 49-56.

[45] S. Stambula, N. Gauquelin, M. Bugnet, S. Gorantla, S. Turner, S. Sun, J. Liu, G. Zhang, X. Sun, G.A. Botton, Chemical structure of nitrogen-doped graphene with single platinum atoms and atomic clusters as a platform for the PEMFC electrode, J. Phys. Chem. C 118 (2014) 3890-3900.

[46] T. Takeda, N. Hirosaki, R.J. Xie, K. Kimoto, M. Saito, Anomalous Eu layer doping in Eu, Si co-doped aluminium nitride based phosphor and its direct observation, J. Mater. Chem. 20 (2010) 9948-9953.

[47] R. Huang, T. Hitosugi, S.D. Findlay, C.A.J. Fisher, Y.H. Ikuhara, H. Moriwake, H. Oki, Y. Ikuhara, Real-time direct observation of Li in $LiCoO_2$ cathode material, Appl. Phys. Lett. 98 (2011) 051913.

[48] R. Huang, Y.H. Ikuhara, T. Mizoguchi, S.D. Findlay, A. Kuwabara, C.A.J. Fisher, H. Moriwake, H. Oki, T. Hirayama, Y. Ikuhara, Oxygen-vacancy ordering at surfaces of lithium manganese(III,IV) oxide spinel nanoparticles, Angew. Chem. Int. Ed. 50 (2011) 3053-3057.

[49] S.Y. Chung, S.Y. Choi, T. Yamamoto, Y. Ikuhara, Atomic-scale visualization of antisite defects in $LiFePO_4$, Phys. Rev. Lett. 100 (2008) 125502.

[50] S.Y. Chung, S.Y. Choi, T. Yamamoto, Y. Ikuhara, Orientation-dependent arrangement of antisite defects in lithium iron(II) phosphate crystals, Angew. Chem. Int. Ed. 121 (2009) 551-554.

[51] Y. Sun, L. Zhao, H. Pan, X. Lu, L. Gu, Y.S. Hu, H. Li, M. Armand, Y. Ikuhara, L. Chen, X. Huang, Direct atomic-scale confirmation of three-phase storage mechanism

in $Li_4Ti_5O_{12}$ anodes for room-temperature sodium-ion batteries, Nat. Commun. 4 (2013) 1870.

[52] F. Wang, H.C. Yu, M.H. Chen, L. Wu, N. Pereira, K. Thornton, A. Van der Ven, Y. Zhu, G.G. Amatucci, J. Graetz, Tracking lithium transport and electrochemical reactions in nanoparticles, Nat. Commun. 3 (2012) 1201.

[53] A. Nie, L.Y. Gan, Y. Cheng, H. Asayesh-Ardakani, Q. Li, C. Dong, R. Tao, F. Mashayek, H.T. Wang, U. Schwingenschlögl, R.F. Klie, R.S. Yassar, Atomic-scale observation of lithiation reaction front in nanoscale SnO_2 materials, ACS Nano 7 (2013) 6203-6211.

[54] G. Van Tendeloo, S. Bals, S. Van Aert, J. Verbeeck, D. Van Dyck, Advanced electron microscopy for advanced materials, Adv. Mater. 24 (2012) 5655-5675.

[55] A.J. D'Alfonso, B. Freitag, D. Klenov, L.J. Allen, Atomic-resolution chemical mapping using energy-dispersive x-ray spectroscopy, Phys. Rev. B 81 (2010) 100101.

[56] N. Braidy, Z.J. Jakubek, B. Simard, G.A. Botton, Quantitative energy dispersive X-ray microanalysis of electron beam-sensitive alloyed nanoparticles, Microsc. Microanal. 14 (2008) 166-175.

[57] K. Kuramochi, T. Yamazaki, Y. Kotaka, M. Ohtsuka, I. Hashimoto, K. Watanabe, Effect of chromatic aberration on atomic-resolved spherical aberration corrected STEM images, Ultramicroscopy 110 (2009) 36-42.

[58] D.O. Klenov, J.M.O. Zide, Structure of the InAlAs/InP interface by atomically resolved energy dispersive spectroscopy, Appl. Phys. Lett. 99 (2011) 141904.

[59] P. Lu, E. Romero, S. Lee, J.L. MacManus-Driscoll, Q. Jia, Chemical quantification of atomic-scale EDS maps under thin specimen conditions, Microsc. Microanal. 20 (2014) 1782-1790.

[60] P. Lu, L. Zhou, M.J. Kramer, D.J. Smith, Atomic-scale chemical imaging and quantification of metallic alloy structures by energy-dispersive X-ray spectroscopy, Sci. Rep. 4 (2014) 3945.

[61] G. Kothleitner, M.J. Neish, N.R. Lugg, S.D. Findlay, W. Grogger, F. Hofer, L.J. Allen, Quantitative elemental mapping at atomic resolution using X-ray spectroscopy, Phys. Rev. Lett. 112 (2014) 085501.

[62] G. Servanton, R. Pantel, M. Juhel, F. Bertin, Two-dimensional quantitative mapping of arsenic in nanometer-scale silicon devices using STEM EELS–EDX spectroscopy, Micron 40 (2009) 543-551.

[63] O.L. Krivanek, M.K. Kundmann, K. Kimoto, Spatial resolution in EFTEM elemental maps, J. Microsc. 180 (1995) 277-287.

[64] B. Schaffer, U. Hohenester, A. Trügler, F. Hofer, High-resolution surface plasmon imaging of gold nanoparticles by energy-filtered transmission electron microscopy, Phys. Rev. B 79 (2009) 041401.

[65] Egerton RF. Electron energy-loss spectroscopy in the electron microscopy. 2nd ed. New York, Plenum Press, 1996.

[66] L.H.G. Tizei, Y. Iizumi, T. Okazaki, R. Nakanishi, R. Kitaura, H. Shinohara, K. Suenaga, Single atom spectroscopy: Decreased scattering delocalization at high energy losses, effects of atomic movement and X-ray fluorescence yield, Ultramicroscopy 160 (2016) 239-246.

[67] X.H. Liu, J.W. Wang, Y. Liu, H. Zheng, A. Kushima, S. Huang, T. Zhu, S.X. Mao, J. Li, S. Zhang, W. Lu, J.M. Tour, J.Y. Huang, In situ transmission electron microscopy of electrochemical lithiation, delithiation and deformation of individual graphene nanoribbons, Carbon 50 (2012) 3836-3844.

[68] W. Xia, Q. Zhang, F. Xu, H. Ma, J. Chen, K. Qasim, B. Ge, C. Zhu, L. Sun, Visualizing the electrochemical lithiation/delithiation behaviors of black phosphorus by in situ transmission electron microscopy, J. Phys. Chem. C 120 (2016) 5861-5868.

[69] Q. Su, D. Xie, J. Zhang, G. Du, B. Xu, In situ transmission electron microscopy observation of the conversion mechanism of Fe_2O_3/graphene anode during lithiation–delithiation processes, ACS Nano 7 (2013) 9115-9121.

[70] X. Ma, M. Zhang, C. Liang, Y. Li, J. Wu, R. Che, Inheritance of crystallographic orientation during lithiation/delithiation processes of single-crystal α-Fe_2O_3 nanocubes in lithium-ion batteries, ACS Appl. Mater. Interfaces 7 (2015) 24191-24196.

[71] W. Xia, Q. Zhang, F. Xu, L. Sun, New insights into electrochemical lithiation/delithiation mechanism of α-MoO_3 nanobelt by in situ transmission electron

microscopy, ACS Appl. Mater. Interfaces 8 (2016) 9170-9177.

[72] F. Hofer, F.P. Schmidt, W. Grogger, G. Kothleitner, Fundamentals of electron energy-loss spectroscopy, IOP Conference Series: Mater. Sci. Eng. 109 (2016) 012007.

[73] Q. Qu, S. Yang, X. Feng, 2D sandwich-like sheets of iron oxide grown on graphene as high energy anode material for supercapacitors, Adv. Mater. 23 (2011) 5574-5580.

[74] S. Shivakumara, T.R. Penki, N. Munichandraiah, Synthesis and characterization of porous flowerlike α-Fe$_2$O$_3$ nanostructures for supercapacitor application, J. Electrochemistry Soc. 2 (2013) A60-A62.

[75] K.J. Lee, S.H. Yu, J.J. Kim, D.H. Lee, J. Park, S.S. Suh, J.S. Cho, Y.E. Sung, Si$_7$Ti$_4$Ni$_4$ as a buffer material for Si and its electrochemical study for lithium ion batteries, J. Power Sources 246 (2014) 729-735.

[76] U. Cvelbar, Z. Chen, M.K. Sunkara, M. Mozetič, Spontaneous growth of superstructure α-Fe$_2$O$_3$ nanowire and nanobelt arrays in reactive oxygen olasma, Small 4 (2008) 1610-1614.

[77] Y. C. Lee, Y. L. Chueh, C.H. Hsieh, M.T. Chang, L.J. Chou, Z.L. Wang, Y.W. Lan, C.D. Chen, H. Kurata, S. Isoda, p-type α-Fe$_2$O$_3$ nanowires and their n-type transition in a reductive ambient, Small 3 (2007) 1356-1361.

[78] Z. Chen, U. Cvelbar, M. Mozetič, J. He, M.K. Sunkara, Long-range ordering of oxygen-vacancy planes in α- Fe$_2$O$_3$ nanowires and nanobelts, Chem. Mater. 20 (2008) 3224-3228.

[79] W. Zhu, J. Winterstein, I. Maimon, Q. Yin, L. Yuan, A.N. Kolmogorov, R. Sharma, G. Zhou, Atomic structural evolution during the reduction of α-Fe$_2$O$_3$ nanowires, J. Phys. Chem. C 120 (2016) 14854-14862.

[80] Y.Y. Fu, R.M. Wang, J. Xu, J. Chen, Y. Yan, A.V. Narlikar, H. Zhang, Synthesis of large arrays of aligned α- Fe$_2$O$_3$ nanowires, Chem. Phys. Lett. 379 (2003) 373-379.

[81] C. Yang, J. Wu, Y. Hou, Fe$_3$O$_4$ nanostructures: synthesis, growth mechanism, properties and applications, Chem. Comm. 47 (2011) 5130-5141.

[82] X. Zhao, D. Xia, K. Zheng, Fe$_3$O$_4$/Fe/Carbon composite and its application as

anode material for lithium-ion batteries, ACS Appl. Mater. Interfaces. 4 (2012) 1350-1356.

[83] F. Niederdraenk, K. Seufert, A. Stahl, R.S. Bhalerao-Panajkar, S. Marathe, S.K. Kulkarni, R.B. Neder, C. Kumpf, Ensemble modeling of very small ZnO nanoparticles, Phys. Chem. Chem. Phys. 13 (2011) 498-505.

[84] T. Ming, W. Feng, Q. Tang, F. Wang, L. Sun, J. Wang, C. Yan, Growth of tetrahexahedral gold nanocrystals with high-index facets, J. Am. Chem. Soc. 131 (2009) 16350-16351.

[85] T.K. Sau, A.L. Rogach, Nonspherical noble metal nanoparticles: colloid-chemical synthesis and morphology control, Adv. Mater. 22 (2010) 1781-1804.

[86] S.H. Lee, S.H. Yu, J.E. Lee, A. Jin, D.J. Lee, N. Lee, H. Jo, K. Shin, T.Y. Ahn, Y.W. Kim, H. Choe, Y.E. Sung, T. Hyeon, Self-assembled Fe_3O_4 nanoparticle clusters as high-performance anodes for lithium ion batteries via geometric confinement, Nano Lett. 13 (2013) 4249-4256.

[87] D. Chen, G. Ji, Y. Ma, J.Y. Lee, J. Lu, Graphene-encapsulated hollow Fe_3O_4 nanoparticle aggregates as a high-performance anode material for lithium ion batteries, ACS Appl. Mater. Interfaces 3 (2011) 3078-3083.

[88] H. Cao, R. Liang, D. Qian, J. Shao, M. Qu, l-serine-assisted synthesis of superparamagnetic Fe_3O_4 nanocubes for lithuium ion batteries, J. Phys. Chem. C 115 (2011) 24688-24695.

[89] X.L. Cheng, J.S. Jiang, D.M. Jiang, Z.J. Zhao, Synthesis of rhombic dodecahedral Fe_3O_4 nanocrystals with exposed high-energy {110} facets and their peroxidase-like activity and lithium storage properties, J. Phys. Chem. C 118 (2014) 12588-12598.

[90] Y. Gan, H. Gu, H. Xiao, Y. Xia, X. Tao, H. Huang, J. Du, L. Xu, W. Zhang, Mesoporous Fe_3O_4@C submicrospheres evolved by a novel self-corrosion mechanism for high-performance lithium-ion batteries, New J. Chem. 38 (2014) 2428-2434.

[91] J. Liu, J. Ni, Y. Zhao, H. Wang, L. Gao, Grapecluster-like Fe_3O_4@C/CNT nanostructures with stable Li-storage capability, J. Mater. Chem. A 1 (2013) 12879-12884.

[92] J.E. Lee, S.H. Yu, D.J. Lee, D.C. Lee, S.I. Han, Y.E. Sung, T. Hyeon, Facile and economical synthesis of hierarchical carbon-coated magnetite nanocomposite particles and their applications in lithium ion battery anodes, Energy Environ. Sci. 5 (2012) 9528-9533.

[93] T.Q. Wang, X.L. Wang, Y. Lu, Q.Q. Xiong, X.Y. Zhao, J.B. Cai, S. Huang, C.D. Gu, J.P. Tu, Self-assembly of hierarchical Fe_3O_4 microsphere/graphene nanosheet composite: towards a promising high-performance anode for Li-ion batteries, RSC Adv. 4 (2014) 322-330.

[94] C. Liang, S. Huang, W. Zhao, W. Liu, J. Chen, H. Liu, Y. Tong, Polyhedral Fe_3O_4 nanoparticles for lithium ion storage, New J. Chem. 39 (2015) 2651-2656.

[95] J. Ouyang, J. Pei, Q. Kuang, Z.X. Xie, L.X. Zheng, Supersaturation-controlled shape evolution of α-Fe_2O_3 nanocrystals and their facet-dependent catalytic and sensing properties, ACS Appl. Mater. Interfaces. 15 (2014) 12505-12514.

[96] M. Čaplovičová, P. Billik, Ľ. Čaplovič, V. Brezová, T. Turáni, G. Plesch, P. Fejdi, On the true morphology of highly photoactive anatase TiO_2 nanocrystals, Appl. Catal. B 117–118 (2012) 224-235.

[97] D.G. Stroppa, L.A. Montoro, A. Beltrán, T.G. Conti, R.O. da Silva, J. Andrés, E. Longo, E.R. Leite, A.J. Ramirez, Unveiling the chemical and morphological features of Sb–SnO_2 nanocrystals by the combined use of high-resolution transmission electron microscopy and ab initio surface energy calculations, J. Am. Chem. Soc. 131 (2009) 14544-14548.

[98] X. Xiaojing, S. Zineb, G. Ralph, M. Günter, Reconstruction of 3D morphology of polyhedral nanoparticles, Nanotechnology 18 (2007) 225501.

[99] R. Zheng, H. Gu, B. Xu, K. K. Fung, X. Zhang, S. P. Ringer, Self-assembly and self-orientation of truncated octahedral magnetite nanocrystals, Adv. Mater. (18) 2006 2418-2421.

[100] W.Z. Zhou, H.F. Greer, What can electron microscopy tell us beyond crystal structures? Eur. J. Inorg. Chem. (2016) 941-950.

[101] F. Fabregat-Santiago, E.M. Barea, J. Bisquert, G.K. Mor, K. Shankar, C.A. Grimes, High carrier density and capacitance in TiO_2 nanotube arrays induced by

electrochemical doping, J. Am. Chem. Soc. 130 (2008) 11312-11316.

[102] X. Lu, G. Wang, T. Zhai, M. Yu, J. Gan, Y. Tong, Y. Li, Hydrogenated TiO_2 nanotube arrays for supercapacitors, Nano Lett. 12 (2012) 1690-1696.

[103] G. Wang, H. Wang, Y. Ling, Y. Tang, X. Yang, R.C. Fitzmorris, C. Wang, J.Z. Zhang, Y. Li, Hydrogen-treated TiO_2 nanowire arrays for photoelectrochemical water splitting, Nano Lett. 11 (2011) 3026-3033.

[104] T. Froschl, U. Hormann, P. Kubiak, G. Kucerova, M. Pfanzelt, C.K. Weiss, R.J. Behm, N. Husing, U. Kaiser, K. Landfester, M. Wohlfahrt-Mehrens, High surface area crystalline titanium dioxide: potential and limits in electrochemical energy storage and catalysis, Chem. Soc. Rev. 41 (2012) 5313-5360.

[105] X. Chen, L. Liu, P.Y. Yu, S.S. Mao, Increasing solar absorption for photocatalysis with black hydrogenated titanium dioxide nanocrystals, Science 331 (2011) 746-750.

[106] J. Qiu, S. Li, E. Gray, H. Liu, Q.F. Gu, C. Sun, C. Lai, H. Zhao, S. Zhang, Hydrogenation synthesis of blue TiO_2 for high-performance lithium-ion batteries, J. Phys. Chem. C 118 (2014) 8824-8830.

[107] C. Liang, L. Liu, H. Li, D. Qian, C. Liu, J. Jia, J. Chen, Microstructural characterization of sulfur-doped Bi_2Te_3 crystals, Mater. Charact. 114 (2016) 172-178.

[108] R. Jin, J. Liu, Y. Xu, G. Li, G. Chen, L. Yang, Hierarchical $Bi_2Se_{3-x}S_x$ microarchitectures assembled from ultrathin polycrystalline nanosheets: solvothermal synthesis and good electrochemical performance, J. Mater. Chem. A 1 (2013) 10942-10950.

[109] N. Shibata, S.D. Findlay, S. Azuma, T. Mizoguchi, T. Yamamoto, Y. Ikuhara, Atomic-scale imaging of individual dopant atoms in a buried interface, Nat. Mater. 8 (2009) 654-658.

[110] J.H. Dycus, R.M. White, J.M. Pierce, R. Venkatasubramanian, J.M. LeBeau, Atomic scale structure and chemistry of Bi_2Te_3/GaAs interfaces grown by metallorganic van der Waals epitaxy, Appl. Phys. Lett. 102 (2013) 081601.

[111] N.V. Tarakina, S. Schreyeck, T. Borzenko, C. Schumacher, G. Karczewski, K. Brunner, C. Gould, H. Buhmann, L.W. Molenkamp, Comparative study of the

microstructure of Bi_2Se_3 thin films grown on Si(111) and InP(111) substrates, Crys. Growth Des. 12 (2012) 1913-1918.

[112] J.S. Lee, A. Richardella, D.W. Rench, R.D. Fraleigh, T.C. Flanagan, J.A. Borchers, J. Tao, N. Samarth, Ferromagnetism and spin-dependent transport in n-type Mn-doped bismuth telluride thin films, Phys. Rev. B 89 (2014) 174425.

[113] J.H. Dycus, J.S. Harris, X. Sang, C.M. Fancher, S.D. Findlay, A.A. Oni, TT.E. Chan, C.C. Koch, J.L. Jones, L.J. Allen, D.L. Irving, J.M. LeBeau, Accurate nanoscale crystallography in real-space using scanning transmission electron microscopy, Microsc. Microanal. 21 (2015) 946-952.

[114] K. Park, Y. Nomura, R. Arita, A. Llobet, D. Louca, Local strain and anharmonicity in the bonding of $Bi_2Se_{3-x}Te_x$ topological insulators, Phys. Rev. B 88 (2013) 224108.

[115] R. Huang, Y. Ikuhara, STEM characterization for lithium-ion battery cathode materials, Curr. Opin. Solid State and Mater. Sci. 16 (2012) 31-38.

[116] Q. Gao, M. Gu, A. Nie, F. Mashayek, C. Wang, G.M. Odegard, R. Shahbazian-Yassar, Direct evidence of lithium-induced atomic ordering in amorphous TiO_2 nanotubes, Chem. Mater. 26 (2014) 1660-1669.

[117] I. Milošv, H.H. Strehblow, B. Navinšek, M. Metikoš-Huković, Electrochemical and thermal oxidation of TiN coatings studied by XPS, Surf. Interface Anal. 23 (1995) 529-539.

[118] B. Avasarala, P. Haldar, Electrochemical oxidation behavior of titanium nitride based electrocatalysts under PEM fuel cell conditions, Electrochim. Acta 55 (2010) 9024-9034.

[119] X. Zhou, C. Shang, L. Gu, S. Dong, X. Chen, P. Han, L. Li, J. Yao, Z. Liu, H. Xu, Y. Zhu, G. Cui, Mesoporous coaxial titanium nitride-vanadium nitride fibers of core–shell structures for high-performance supercapacitors, ACS Appl. Mater. Interfaces 3 (2011) 3058-3063.

[120] S. Dong, X. Chen, L. Gu, X. Zhou, H. Wang, Z. Liu, P. Han, J. Yao, L. Wang, G. Cui, L. Chen, TiN/VN composites with core/shell structure for supercapacitors, Mater. Res. Bull. 46 (2011) 835-839.

[121] J.J. Friel, C.E. Lyman, Tutorial Review: X-ray mapping in electron-beam instruments, Microsc. Microanal. 12 (2006) 2-25.

[122] K.X. Wang, X.H. Li, J.S. Chen, Surface and interface engineering of electrode materials for lithium-ion batteries, Adv. Mater. 27 (2015) 527-545.

[123] F. Masayuki, C. Ikung, K. Yuju, K. Satoshi, S. Tatsuo, M. Hiroaki, Synthesis of TiN–BaTiO$_3$ core–shell structured ceramics: A new approach to ferroelectric thin-film formation, Appl. Phys. Express 8 (2015) 015501.

[124] S. Dong, X. Chen, L. Gu, X. Zhou, L. Li, Z. Liu, P. Han, H. Xu, J. Yao, H. Wang, X. Zhang, C. Shang, G. Cui, L. Chen, One dimensional MnO$_2$/titanium nitride nanotube coaxial arrays for high performance electrochemical capacitive energy storage, Energy Environ. Sci. 4 (2011) 3502-3508.

[125] X. Wang, V. Raju, W. Luo, B. Wang, W.F. Stickle, X. Ji, Ambient hydrolysis deposition of TiO$_2$ in nanoporous carbon and the converted TiN-carbon capacitive electrode, J. Mater. Chem. A 2 (2014) 2901-2905.

[126] H. Zheng, S. Fang, Z. Tong, G. Pang, L. Shen, H. Li, L. Yang, X. Zhang, Stabilized titanium nitride nanowire supported silicon core-shell nanorods as high capacity lithium-ion anodes, J. Mater. Chem. A 3 (2015) 12476-12481.

[127] J.Y. Liao, D. Higgins, G. Lui, V. Chabot, X. Xiao, Z. Chen, Multifunctional TiO$_2$–C/MnO$_2$ core–double-shell nanowire arrays as high-performance 3D electrodes for lithium ion batteries, Nano Lett. 13 (2013) 5467-5473.

[128] O. Tunckan, H. Yurdakul, S. Turan, Identification and quantification of reaction phases at Si$_3$N$_4$–Ti interfaces by using analytical transmission electron microscopy techniques, Ceram. Int. 39 (2013) 1087-1095.

[129] X. Lu, T. Liu, T. Zhai, G. Wang, M. Yu, S. Xie, Y. Ling, C. Liang, Y. Tong, Y. Li, Improving the cycling stability of metal–nitride supercapacitor electrodes with a thin carbon shell, Adv. Energy Mater. 4 (2014) 1300994.

[130] M. Zhi, C. Xiang, J. Li, M. Li, N. Wu, Nanostructured carbon-metal oxide composite electrodes for supercapacitors: a review, Nanoscale 5 (2013) 72-88.

[131] L. Shen, E. Uchaker, X. Zhang, G. Cao, Hydrogenated Li$_4$Ti$_5$O$_{12}$ nanowire arrays for high rate lithium ion batteries, Adv. Mater. 24 (2012) 6502-6506.

[132] Z.L. Wang, J. Bentley, N.D. Evans, Mapping the valence states of transition-metal elements using energy-filtered transmission electron microscopy, J. Phys. Chem. B 103 (1999) 751-753.

[133] H. Tan, J. Verbeeck, A. Abakumov, G. Van Tendeloo, Oxidation state and chemical shift investigation in transition metal oxides by EELS, Ultramicroscopy 116 (2012) 24-33.

[134] Z.L. Wang, J.S. Yin, Y.D. Jiang, J. Zhang, Studies of Mn valence conversion and oxygen vacancies in $La_{1-x}Ca_xMnO_{3-y}$ using electron energy-loss spectroscopy, Appl. Phys. Lett. 70 (1997) 3362-3364.

[135] S. Estradé, L. Yedra, A. López-Ortega, M. Estrader, G. Salazar-Alvarez, M.D. Baró, J. Nogués, F. Peiró, Distinguishing the core from the shell in MnOx/MnOy and FeOx/MnOx core/shell nanoparticles through quantitative electron energy loss spectroscopy (EELS) analysis, Micron 43 (2012) 30-36.

[136] T. Zhai, S. Xie, M. Yu, P. Fang, C. Liang, X. Lu, Y. Tong, Oxygen vacancies enhancing capacitive properties of MnO_2 nanorods for wearable asymmetric supercapacitors, Nano Energy 8 (2014) 255-263.

[137] L.A.J. Garvie, A.J. Craven, High-resolution parallel electron energy-loss spectroscopy of Mn $L_{2,3}$-edges in inorganic manganese compounds, Phys. Chem. Miner. 21 (1994) 191-206.

[138] H.K. Schmid, W. Mader, Oxidation states of Mn and Fe in various compound oxide systems, Micron 37 (2006) 426-432.

[139] C.C. Appel, G.A. Botton, A. Horsewell, W.M. Stobbs, Chemical and structural changes in manganese-doped yttria-stabilized zirconia studied by electron energy loss spectroscopy combined with electron diffraction, J. Am. Ceram. Soc. 82 (1999) 429-435.

[140] T. Riedl, T. Gemming, K. Wetzig, Extraction of EELS white-line intensities of manganese compounds: methods, accuracy, and valence sensitivity, Ultramicroscopy 106 (2006) 284-291.

[141] H. Kurata, E. Lefèvre, C. Colliex, R. Brydson, Electron-energy-loss near-edge structures in the oxygen K-edge spectra of transition-metal oxides, Phys. Rev. B. 47

(1993) 13763-13768.

[142] H. Kurata, C. Colliex, Electron-energy-loss core-edge structures in manganese oxides, Phys. Rev. B 48 (1993) 2102-2108.

[143] S.D. Perera, B. Patel, N. Nijem, K. Roodenko, O. Seitz, J.P. Ferraris, Y.J. Chabal, K.J. Balkus, Vanadium oxide nanowire–carbon nanotube binder-free flexible electrodes for supercapacitors, Adv. Energy Mater. 1 (2011) 936-945.

[144] S. Lee, C. Cheng, H. Guo, K. Hippalgaonkar, K. Wang, J. Suh, K. Liu, J. Wu, Axially engineered metal–insulator phase transition by graded doping VO_2 nanowires, J. Am. Chem. Soc. 135 (2013) 4850-4855.

[145] W. Zhao, Q. Zhong, Y. Pan, R. Zhang, Systematic effects of S-doping on the activity of V_2O_5/TiO_2 catalyst for low-temperature NH_3-SCR, Chem. Eng. J 228 (2013) 815-823.

[146] H. Asayesh-Ardakani, A. Nie, P.M. Marley, Y. Zhu, P.J. Phillips, S. Singh, F. Mashayek, G. Sambandamurthy, K. Low, R.F. Klie, S. Banerjee, G.M. Odegard, R. Shahbazian-Yassar, Atomic origins of monoclinic-tetragonal (rutile) phase transition in doped VO_2 nanowires, Nano Lett. 15 (2015) 7179-7188.

[147] T. Zhai, X. Lu, Y. Ling, M. Yu, G. Wang, T. Liu, C. Liang, Y. Tong, Y. Li, A new benchmark capacitance for supercapacitor anodes by mixed-valence sulfur-doped V_6O_{13-x}, Adv. Mater. 26 (2014) 5869-5875.

[148] Y. Ishiwata, E. Takahashi, K. Akashi, M. Imamura, J. Azuma, K. Takahashi, M. Kamada, H. Ishii, Y.F. Liao, Y. Tezuka, Y. Inagaki, T. Kawae, D. Nishio-Hamane, M. Nantoh, K. Ishibashi, T. Kida, Impurity-induced first-order phase transitions in highly crystalline V_2O_3 nanocrystals, Adv. Mater. Interfaces 2 (2015) 1500132.

High lights

- Analyzing structural characteristics of transition metal compound anode by TEM

- Vacancy defect structures and dopant distributions were investigated by HR(S)TEM.

- Valence state of transition metal elements was analyzed by EELS

- Chemical information of complex structures was obtained by elemental mapping.